Hybrid CoPc/Cu-Based core-shell nanocatalyst for exploring electrocatalytic tandem effect in CO_2RR

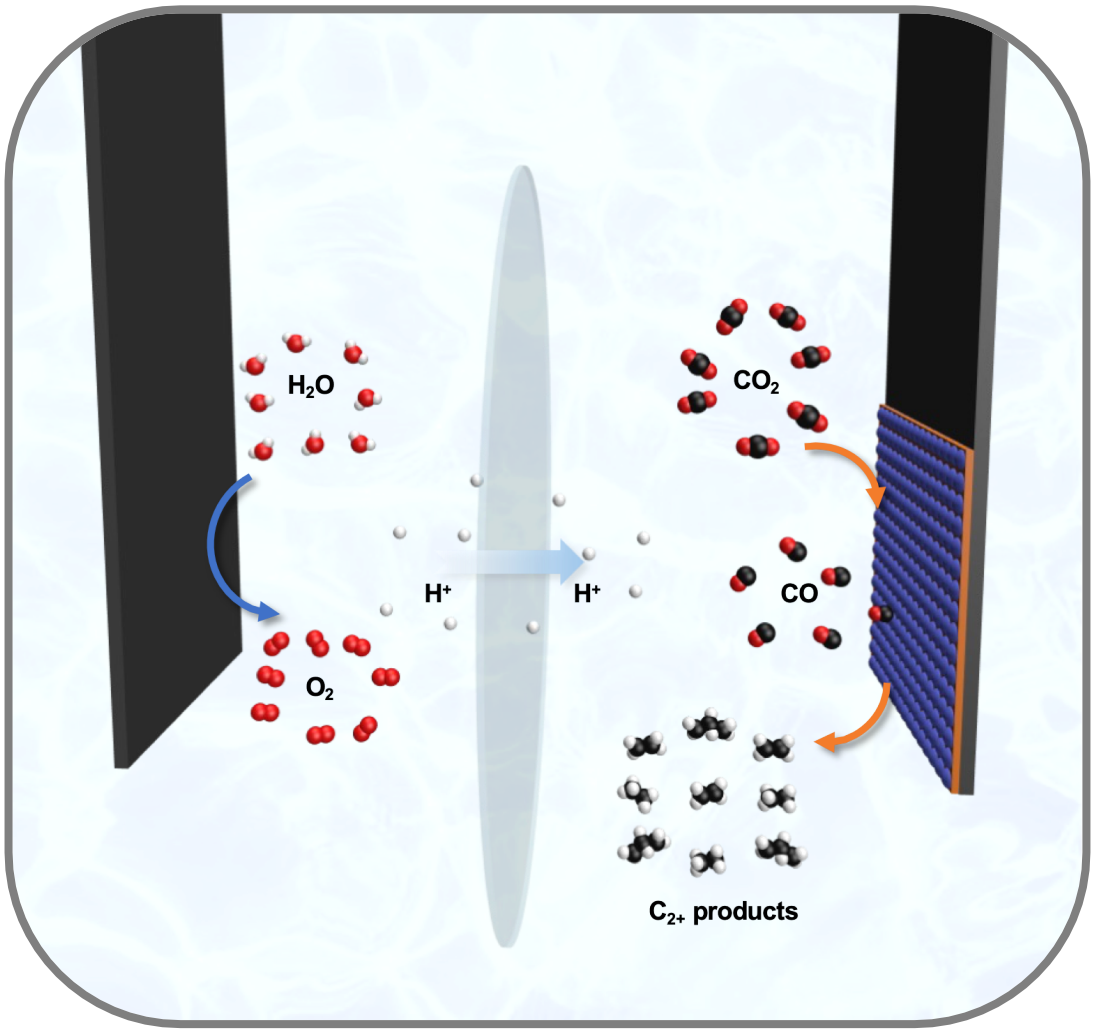

Supervised by Prof. Emilio Palomares and Joan Marc Bondia

ICIQ Institute of Chemical Research of Catalonia

UNIVERSITAT ROVIRA i VIRGILI
Dept. de Química Analítica
i Química Orgànica

Marta Grados Rion

Master in Synthesis Catalysis and Molecular Design (2024-2025)

ABSTRACT

In recent years, there has been an increase in the release of carbon emissions into the atmosphere, which has led to a direct dramatic impact on global warming and environmental issues. This has pushed the scientific community to accelerate the development of innovative technologies for reducing CO_2 emissions.

Given these findings, this research focuses on the transformation of CO_2 into sustainable chemicals and fuels using copper-based nanocatalysts. The inherent property of copper to absorb CO intermediates and promote the C-C coupling step for the formation of C_{2+} products makes copper a unique catalyst, capable of producing multi-carbon products. However, the copper-based catalysts exhibit low selectivity, as they can produce a wide range of products, including C_1 (mainly CO and HCOO-) and C_{2+} products (especially C_2H_4 and C_2H_5OH). One strategy to boost the selectivity involves designing dual-site tandem catalysts, where a CO_2-to-CO selective co-catalyst supplies CO molecules to copper sites, thereby facilitating C-C dimerization.
In this context, a core-shell system was synthesized, encapsulating Cu_2O NCs with a polymeric coating formed via an azide-alkyne "click" reaction between tetra-azido substituted cobalt (II) phthalocyanine (CoPc) – a well-known compound for its high selectivity towards CO production – and alkyne-substituted monomers.

The study explores the effect of a hybrid CoPc/Cu-based core-shell system in the electrocatalytic reduction of CO_2 for the selective conversion into valuable industrial products, identifying the parameters that have the greatest impact on selectivity and activity.

INDEX

1. OBJECTIVES

The primary objective of this research is to create copper-based hybrid nanocubes integrated with CoPc-based polymers to enhance tandem electrochemical CO_2 reduction. This involves designing a core–shell structure, where Cu_2O nanocubes serve as the catalytic core for carbon–carbon (C–C) coupling, while CoPc-based polymers form the outer shell responsible for the CO generation. The work specifically aims at synthesizing and assembling hybrid catalysts using two polymer variants, CoPc_2alk and CoPc_3alk, and investigating how their structural differences affect morphology and catalytic performance. We also evaluate the electrochemical performance of the resultant materials, focusing on CO reduction activity, selectivity, and the distribution of C_{2+} products. Furthermore, analyze the tandem catalytic effect, with special attention to how CO diffusion from the polymer shell enhances C–C coupling processes at the Cu core.

2. INTRODUCTION

The persistent rise in atmospheric carbon dioxide (CO_2) levels, primarily driven by the combustion of fossil fuels and various industrial activities, poses a serious threat to global climate stability, highlighting an urgent need for innovative solutions.[1] In response to this challenge, the electrochemical CO_2 reduction reaction (CO_2RR) powered by renewable energy has emerged as a promising technology that not only helps to mitigate greenhouse gas emissions but also facilitates the sustainable production of valuable fuels and chemicals. [1,2]

The electrochemical CO_2RR involves the conversion of CO_2 into a wide array of products, ranging from single-carbon (C_1) compounds such as carbon monoxide (CO), formic acid, methane, and methanol, to more complex multi-carbon (C_{2+}) products including ethylene, ethanol, propanol, and others as shown in Table 1. However, the inherent chemical stability of the CO_2 molecule and the significant energy barrier associated with its activation pose major challenges for efficient electrochemical conversion. To overcome these impediments, transition metal-based catalysts are commonly employed to lower the overpotential and accelerate the reaction kinetics. These transformations require multiple coupled proton-electron transfer steps, with the

selectivity and efficiency being highly dependent on the nature of the electrocatalyst and the local reaction environment. In fact, it is well-known that the CO_2RR products distribution is primarily governed by the relative adsorption energies of *CO (where the asterisk denotes adsorption at an active site on the metal surface). Weak *CO binding energies typically facilitates its desorption, leading to CO formation. In contrast, overly strong CO adsorption can result in catalyst deactivation due to surface poisoning. Nevertheless, with moderate *CO binding energies, the CO intermediate can be sufficiently stable to participate in subsequent electrochemical transformations. [1,3,4]

Table 1. Electrocatalytic CO_2RR reactions

Reaction	E⁰ [V vs RHE]	(Product) Name, abbreviation
$2H_2O \rightarrow O_2 + 4H^+ + 4e^-$	1.23	Oxygen Evolution Reaction, OER
$2H^+ + 2e^- \rightarrow H_2$	0	Hydrogen Evolution Reaction, HER
$xCO_2 + nH^+ + ne^- \rightarrow$ product $+ yH_2O$	-	*CO_2 Reduction, CO_2R*
$CO_2 + 2H^+ + 2e^- \rightarrow HCOOH$ (aq)	–0.12	Formic acid
$CO_2 + 2H^+ + 2e^- \rightarrow CO(g) + H_2O$	–0.10	Carbon monoxide
$CO_2 + 6H^+ + 6e^- \rightarrow CH_3OH$ (aq) $+ H_2O$	0.03	Methanol
$CO_2 + 8H^+ + 8e^- \rightarrow CH_4(g) + 2H_2O$	0.17	Methane
$2CO_2 + 8H^+ + 8e^- \rightarrow CH_3COOH$ (aq) $+ 2H_2O$	0.11	Acetic acid
$2CO + 12H^+ + 12e^- \rightarrow C_2H_5OH$ (aq) $+ 3H_2O$	0.09	Ethanol
$2CO + 12H^+ + 12e^- \rightarrow C_2H_4(g) + 4H_2O$	0.08	Ethylene
$2CO + 14H^+ + 14e^- \rightarrow C_2H_6(g) + 4H_2O$	0.14	Ethane
$3CO_2 + 16H^+ + 16e^- \rightarrow C_3H_6CHO$ (aq) $+ 5H_2O$	0.09	Propionaldehyde
$3CO_2 + 18H^+ + 18e^- \rightarrow C_3H_7OH$ (aq) $+ 5H_2O$	0.10	Propanol

Most of the transition metal-based catalysts primarily facilitate the two-electron reduction pathway, resulting in CO as the dominant product.[4–6] However, in recent years, copper (Cu) has been the most extensively studied metal for the electrochemical reduction of CO_2 due to its unique catalytic properties; it exhibits distinctive catalytic behavior that enables carbon–carbon (C–C) bond formation. [3] This intrinsic property facilitates the production of multi-carbon (C_{2+}) products such as oxygenates and hydrocarbons, owing to copper's unique ability to *CO and *OCHO intermediate, which is crucial to promote complex electrochemical transformations that are often inaccessible with other monometallic catalysts.[4] Conversely, achieving high selectivity and energy efficiency in

these transformations remains challenging, primarily due to competing side reactions like the hydrogen evolution reaction (HER), (Table 1), which intensifies over time, owing to morphological transformations that copper-based materials suffer under cathodic conditions, ultimately leading to reduced CO_2RR. [1,6]

Gaining insight into the electrocatalytic conversion of CO_2 into multi-carbon products using copper catalyst is essential for designing new materials with improved activity and selectivity. Some works claim that this reaction proceeds through a complex sequence of elementary steps on copper (Cu) surfaces, which is crucial in determining product selectivity. For instance, Cu (111) facets are attributed to methane formation, especially at high overpotentials. In contrast, Cu (100) surfaces tend to produce more C_2 products, particularly at lower overpotentials. Moreover, DFT studies suggest that the (100) and (211) surface facets, which are predominant in Cu_2O nanocubes (NCs), exhibit higher selectivity towards C_{2+} products, where C-C coupling is favored. However, despite revealing the structural features that promote multi-carbon product formation, this understanding alone appears insufficient to achieve high FE for a desired product. [7,8]

A key strategy to enhance C–C bond formation and increase selectivity for C_{2+} products is tandem catalysis, where two complementary catalytic domains work together to facilitate multistep transformations. [5] Here, in Figure 1 the CO is generated in proximity and diffuses into the Cu interface, where C-C coupling reaction and further reduction into C_{2+} products can take place.

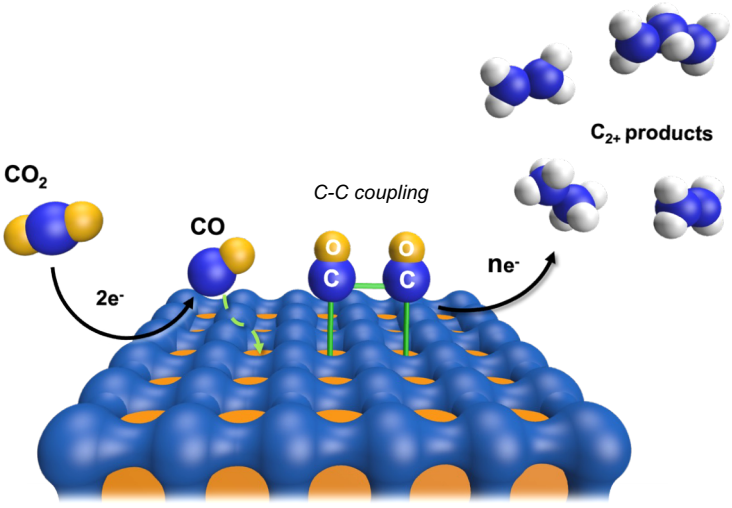

Figure 1. Tandem catalysis scheme.

For instance, the combination of an organometallic molecular catalyst for CO_2RR to CO with Cu-based materials has emerged as a promising strategy to enhance the efficiency and selectivity of CO_2RR. These hybrid systems operate via cooperative mechanisms, where the molecular component serves as a CO-selective catalytic site, enhancing the efficiency of the initial two-electron CO_2-to-CO reduction and increasing local CO concentration at the Cu sites to facilitate the subsequent CO dimerization step.

Several studies in the literature have explored tandem catalysis involving cobalt phthalocyanine integrated with a Cu-based catalyst. In particular, Wang et al. study, achieves a FE_{C2+} of 73.17%, and the FE for ethylene of 52.35% at −1.26 V_{RHE}. The incorporation of catalytically active cobalt phthalocyanine (CoPc) moieties significantly enhances local *CO coverage. This localized enrichment effectively lowers the activation barrier for the C–C coupling step at Cu^+ active sites, facilitating the efficient dimerization of CO intermediates and promoting the selective formation of C_{2+} products.[3]

As mentioned above, the key step in achieving tandem catalysis is to develop a well-defined CO_2-to-CO selective co-catalyst, which must be effectively coupled with copper. For instance, CoPc shown in Figure 2, is a well-established molecular catalyst for the electrochemical CO_2RR to CO, owing to its robust redox activity and ability to stabilize key reaction intermediates, making it a promising candidate for this role. [3]

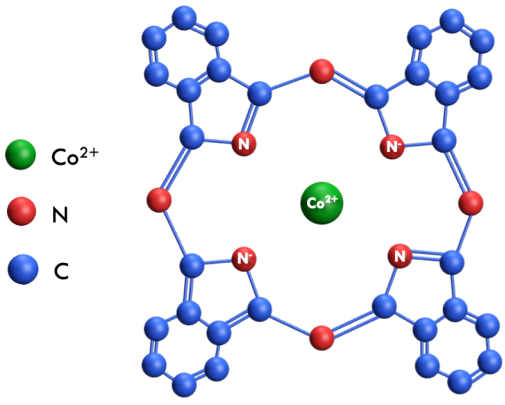

Figure 2. Cobalt phthalocyanine molecule.

In Figure 3, a catalytic cycle for CO conversion by the CoPc is proposed. This catalytic pathway begins with the one-electron reduction of the Co (II) to Co(I), the reduced complex with the CO_2 generates Co–CO_2^- intermediate, which, with protonation, forms a Co–COOH species. A second electron transfer facilitates the cleavage of the C–O bond, yielding a Co–CO intermediate and releasing a hydroxide ion (OH^-). Consequently, CO is released from the metal center, and the CoPc catalyst is regenerated through interaction with water and additional proton and electron exchange, completing the catalytic cycle.[9,10]

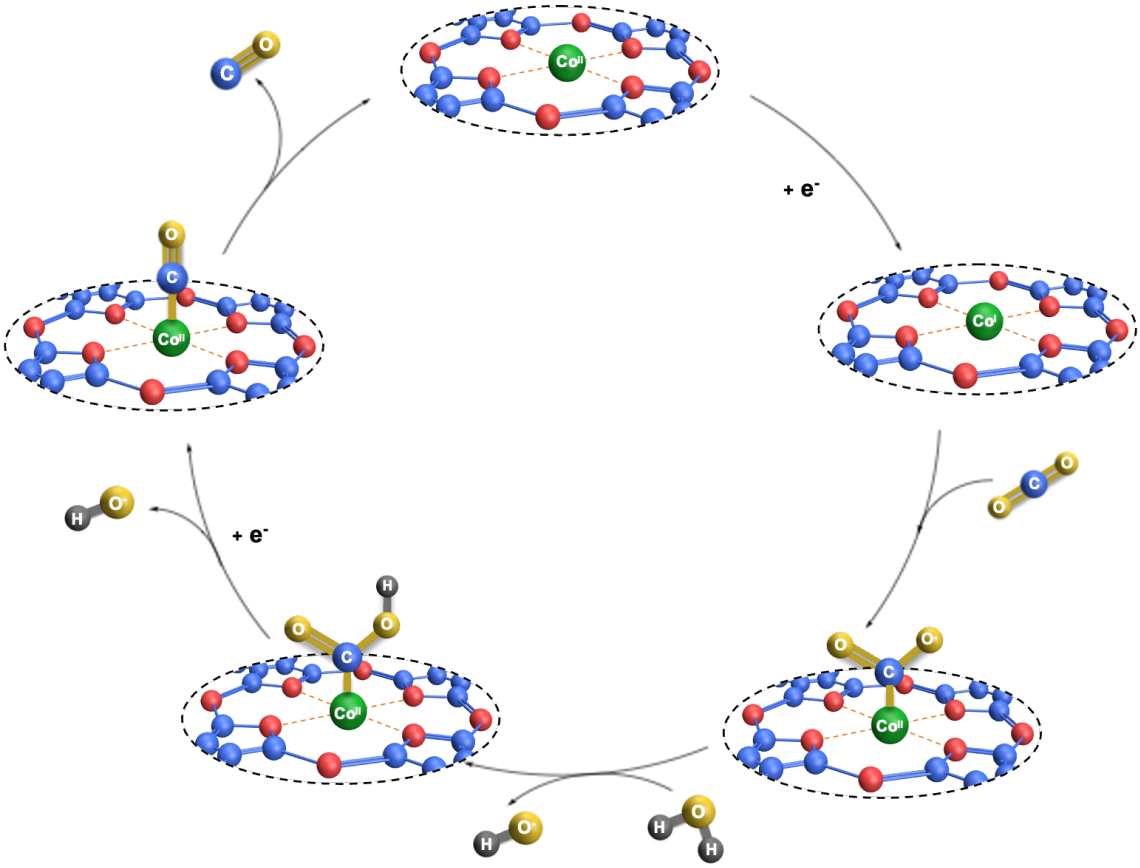

Figure 3. Catalytic cycle of CO_2 to CO conversion by CoPc. [10]

Nevertheless, a significant challenge associated with CoPc and similar planar macrocyclic systems is their tendency to undergo intermolecular π–π stacking interactions (Figure 4), leading to aggregation and reducing the catalytic activity due to the limited electroactive surface area.[11]

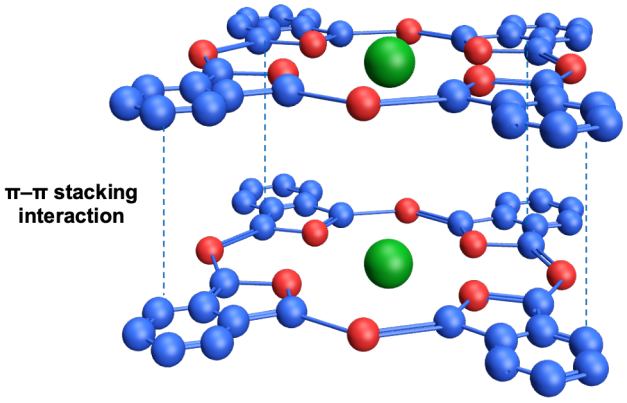

Figure 4. Scheme CoPc π–π stacking interactions.

A viable strategy to overcome this issue involves dispersing the CoPc molecules onto a high-surface-area support material such as carbon nanotubes (CNTs), incorporated into the catalyst matrix (Figure 5). CNTs increase the surface area, improve the control of spatial distribution, prevent aggregation, and enhance electron transport throughout the catalytic film. This strategy improves catalyst utilization and contributes to better long-term stability and activity. [12]

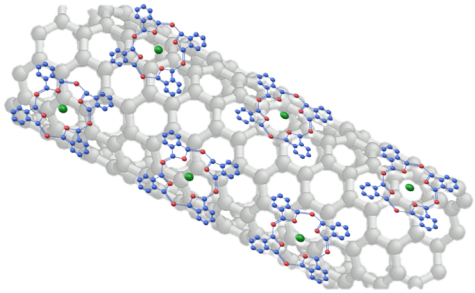

Figure 5. CoPc dispersed onto CNTs.

Accordingly, the CO formation from CO_2, to then understand the CO transformation further to multicarbon products. The proposed mechanism begins with the adsorption of CO on metallic Cu, as is shown in Figure 6. The primary C-C coupling pathway involves the dimerization of two adjacent *CO molecules to form the *OCCO intermediate, a step identified as rate-determining step for most C_{2+} products.[7,13]

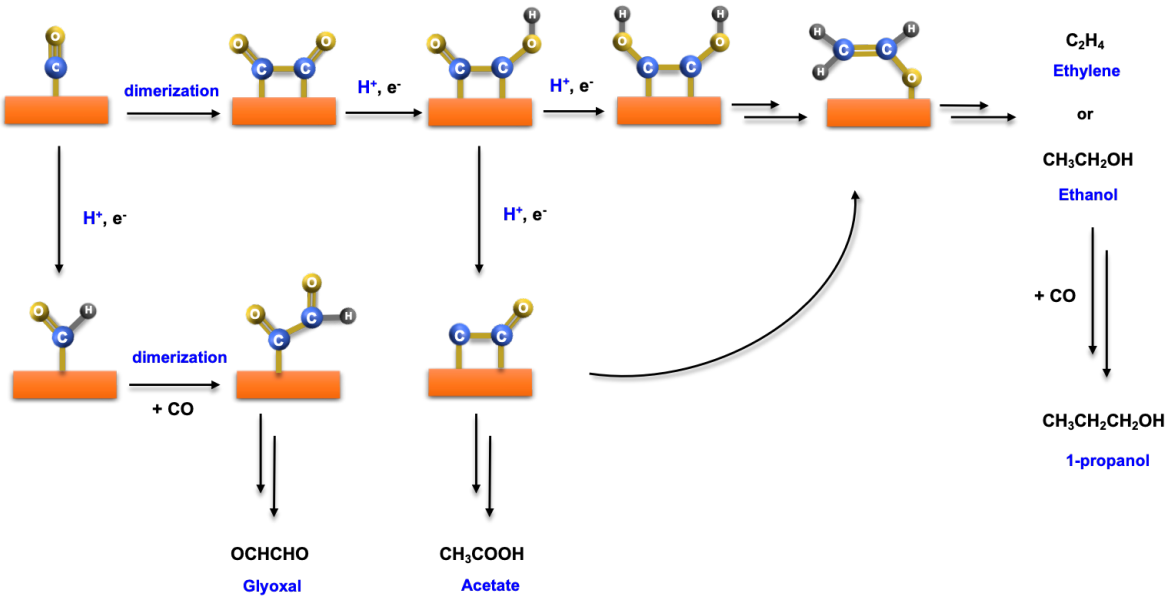

Figure 6.Proposed pathways for C-C coupling in CO_2RR.[7]

In view of these findings, to explore the tandem catalytic effect, this research starts with the synthesis of two cobalt (II) phthalocyanine-containing polymers. One with two alkyl groups, CoPc_2alk, and the other with three, CoPc_3alk, to compare the influence of the steric conformation, via a "click" polymerization reaction based on Cu(I)-catalyzed azide–alkyne cycloaddition (CuAAC), as is shown in Figure 7.[14,15]

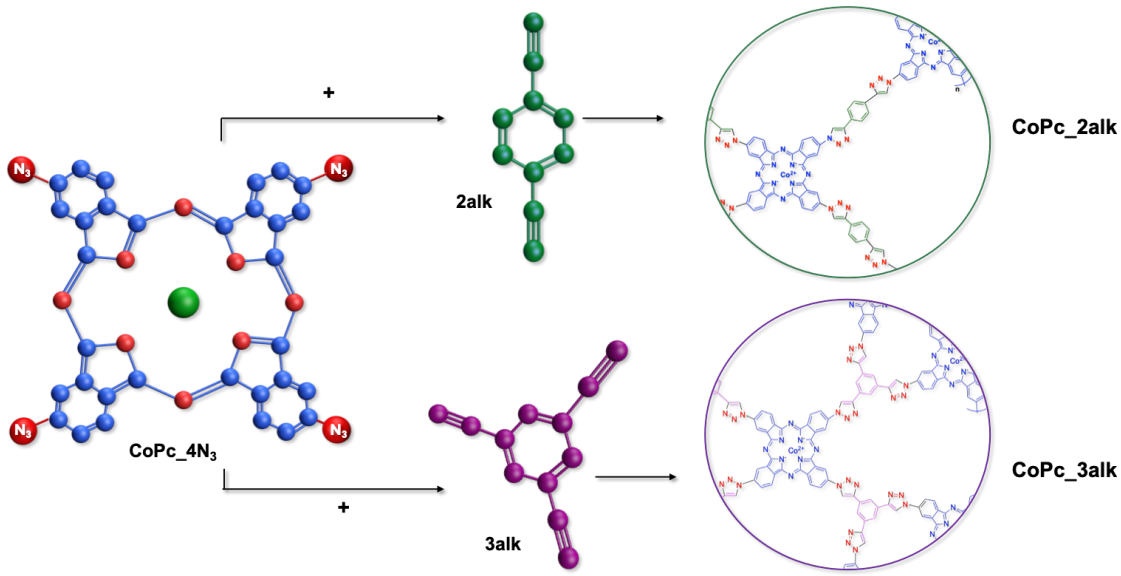

Figure 7. CuAAC polymerization reaction.

The hybrid materials were synthesized using the same strategy. However, in this case, the Cu_2O NCs served as both catalyst and template for the CuAAC reaction, leading to well-defined core-shell hybrid catalysts: Cu_2O@CoPc_2alk and Cu_2O@CoPc_3alk (Figure 8). To examine the influence of catalyst dispersion, all materials were also explored with CNTs, for the assessment of how aggregation affects the overall catalytic activity and the efficacy of the tandem mechanism. This study aims to assess the possible CO diffusion limitations by using core-shell systems, which not only may ensure efficient CO generation but also may optimize molecular transport and interfacial communication between catalytic domains.

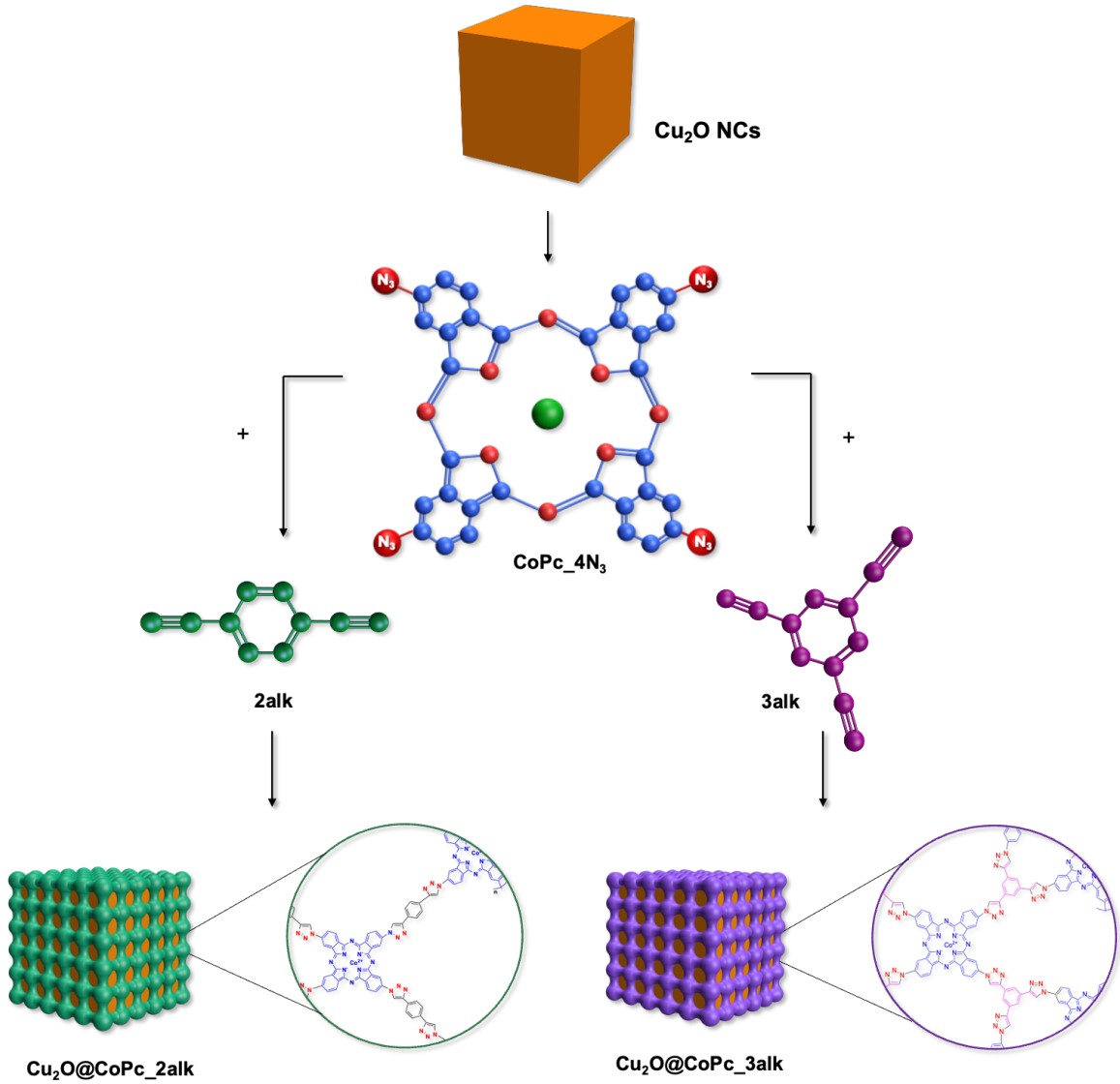

Figure 8. CuAAC polymerization reaction templated onto Cu_2O NCs.

3. EXPERIMENTAL SECTION

3.1 REAGENTS AND MATERIALS

The reagents and solvents used in the synthesis of the Cu_2O NCs, the monomer cobalt (II) tetraazide phthalocyanine, the polymers, and the hybrid materials are:

The trisodium citrate dehydrate ($C_6H_9Na_3O_9$), copper (II) sulfate (Cu_2SO_4), sodium hydroxide (NaOH), ascorbic acid ($C_6H_8O_6$), copper (II) hydroxide ($Cu(OH)_2$), cobalt (II) tetraminophthalocyanine ($C_{32}H_{20}CoN_{12}$), p-toluenesulfonic acid ($CH_3C_6H_4SO_3H$), sodium nitrite ($NaNO_2$), sodium azide (NaN_3), dimethyl formamide (DMF), sodium ascorbate ($C_6H_7NaO_6$), ethanol (C_2H_6O), tetrahydrofuran (THF), 1,3,5-triethynylbenzene ($C_{12}H_6$), 1,4-diethylbenzene ($C_{10}H_6$), acetone (C_3H_6O), dichloromethane (CH_2Cl_2), diethyl ether ($(CH_3CH_2)_2O$).

3.2 SYNTHESIS

3.2.1 Synthesis copper(I) nanocubes (Cu_2O NCs)

Cu_2O NCs were prepared following the synthetic procedures already reported in the literature.[15] In a 500 mL Erlenmeyer flask, 2 mL of a 0.9 M aqueous solution of trisodium citrate dehydrate ($C_6H_9Na_3O_9$) was added to 400 mL of water. This compound is used in the synthesis to prevent nanoparticles from agglomerating and merging into bigger particles. After stirring for 20 minutes, 2 mL of a 1.2 M aqueous solution of $CuSO_4$ was added, and the mixture was stirred for an additional 5 minutes. Then, 2 mL of a 4.8 M aqueous solution of NaOH was added to the mixture, which then turned a more intense color and became turbid. These changes indicate the formation of less soluble Cu $(OH)_2$. After stirring for 5 more minutes, 2 mL of a 1.2 M aqueous ascorbic acid solution was added. A color change from blue to orange was observed, hinting the formation of Cu_2O NCs and the complete reduction of the Cu^{2+} ions to Cu^{+}. After stirring for 30 minutes at room temperature, Cu_2O NCs were collected by centrifugation and washed with water, 1:1 mixture of water: ethanol, and ethanol. Finally, the Cu_2O NCs were dried under vacuum before use.

3.2.2 Synthesis of cobalt (II) tetraazide phthalocyanine (CoPc_4N_3)

Co (II) tetraminophthalocyanine (100 mg, 0.158 mmol) was dissolved in 6 mL of water along with p-toluenesulfonic acid (1.08 g, 5.7 mmol). Next, a sodium nitrite ($NaNO_2$, 0.39 g, 5.7 mmol) solution was added dropwise to the mixture and stirred for 1 hour. Afterward, sodium azide (NaN_3, 65.8 mg, 1.01 mmol) was added, and the reaction continued for an additional 1 hour and 30 minutes. The resulting dark green solid was then washed with water, filtered, and dried in the oven.

3.2.3 Synthesis of the polymers

The CoPc-based polymers were prepared by following a modified reported procedure: [14]

CoPc_3alk: 15 mg of CoPc_4N_3 ($2\cdot10^{-2}$mmol) was weighed in a sealed vial and dissolved in 2 mL of DMF. Then, the solution was sonicated for 10 to 15 minutes. Separately, 4.01 mg ($2.67\cdot10^{-2}$ mmol) of 1,3,5-triethynylbenzene, 2.17 mg (0.02mmol) of $CuSO_4$, and 4.55 mg of sodium ascorbate ($2.3\cdot10^{-2}$ mmol) were added to the CoPc_4N_3 solution. After bubbling the vial with argon for 30 minutes, the reaction was left under stirring at 100°C overnight. Finally, the corresponding polymer was filtered (under vacuum using a Teflon filter (0.2 μm pore, 25 mm diameter)), washed with water, ethanol, and THF, and dried in the oven.

CoPc_2alk: 15 mg of CoPc_4N_3 (0.02 mmol) was weighed in a sealed vial and dissolved in 2 mL of DMF. Then, the solution was sonicated for 10 to 15 minutes. Separately, 5.05 mg (0.04 mmol) of 1,4-diethynylbenzene, 2.17 mg (0.02mmol) of $CuSO_4$, and 4.53 mg of sodium ascorbate ($2.3\cdot10^{-2}$ mmol) were added to the CoPc_4N_3 solution. After bubbling the vial with argon for 30 minutes, the reaction was left under stirring at 100°C overnight. Finally, the corresponding polymer was filtered (under vacuum using a Teflon filter (0.2 μm pore, 25 mm diameter)), washed with water, ethanol, and THF, and dried in the oven.

3.2.4 Synthesis of the hybrid materials

The hybrid Cu_2O NCs were prepared by following a modified reported procedure: [15]

Cu_2O@CoPc_3alk: 40 mg of Cu_2O NCs were weighed and dispersed in 10 mL of DMF within a sealed vial, then bubbled with Ar for 15 minutes. The suspension was sonicated for 15 minutes to ensure good dispersion. Separately, 6.37 mg (0.00866 mmol) of cobalt (II) phthalocyanine bearing azide groups (CoPc_4N_3) and 1.73 mg ($1.15 \cdot 10^{-2}$ mmol) of 1,3,5-triethynylbenzene were dissolved in the minimal volume of DMSO (approximately 1–2 mL) in a different vial. Simultaneously, both solutions were added to the reaction mixture under an inert atmosphere, with continuous argon bubbling for 10 minutes. Finally, the reaction was then stirred for 20 hours at room temperature, in the dark. The resulting Cu_2O@CoPc_2alk nanoparticles were collected via centrifugation and then washed with different solvents: DMSO, acetone, dichloromethane (CH_2Cl_2), and diethyl ether to remove unreacted species. The purified product was dried under vacuum before further characterization.

Cu_2O@CoPc_2alk: 40 mg of Cu_2O NCs were weighed and dispersed in 10 mL of DMF within a sealed vial, then bubbled with Ar for 15 minutes. The suspension was sonicated for 15 minutes to ensure good dispersion. Separately, 6.43 mg ($8.66 \cdot 10^{-3}$ mmol) of cobalt (II) phthalocyanine bearing azide groups (CoPc_4N_3) and 2,1849 mg ($1.73 \cdot 10^{-2}$ mmol) of 1,4-diethynylbenzene were dissolved in the minimal volume of DMF (approximately 1–2 mL) in a different vial. Simultaneously, both solutions were added to the reaction mixture with continuous argon bubbling for 10 minutes. Finally, the reaction was then stirred for 20 hours at room temperature, in the dark. The resulting Cu_2O@CoPc_2alk nanoparticles were collected via centrifugation and then washed with different solvents: DMF, acetone, dichloromethane (CH_2Cl_2), and diethyl ether in order to remove the unreacted species. The purified product was dried under vacuum before further characterization.

3.3 ELECTROCATALYTIC PERFORMANCE

Figure 9 illustrates an H-cell, where the working electrode, made of Toray Carbon Paper (TGP-H-60, Alfa-Aesar) as the support material, and a leak-free Ag/AgCl electrode (Alvatek) as the reference electrode are located in the cathodic compartment. In contrast, a carbon rod (XRD Graphite Manufacturing Co., Ltd) was used as the counter electrode, positioned in the anodic compartment. An anion-exchange membrane (Selemion AMV, AGC Engineering) separates the cathode from the anode, preventing product crossover between the two individual cells.

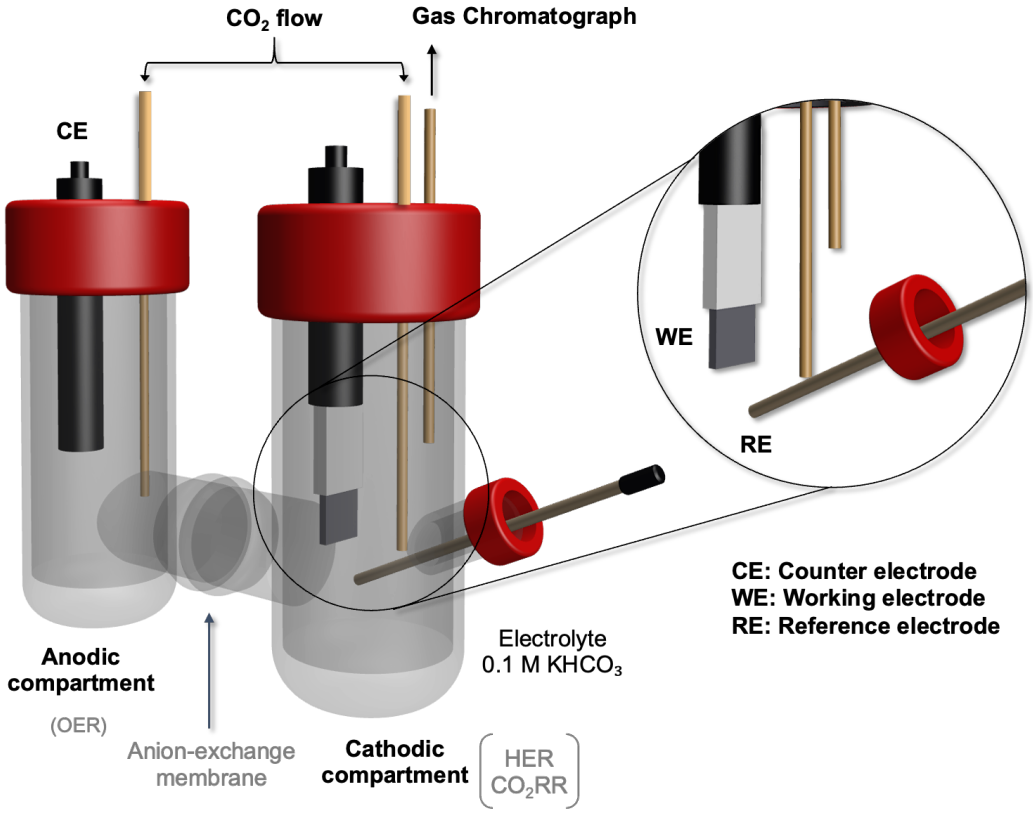

Figure 9. H-cell setup scheme.

The electrochemical reactions were performed under a CO_2 flow of 30 mL/min, controlled by a mass flow controller. The experiment begins with the addition of 18 mL of the electrolyte 0.1M $KHCO_3$ to each compartment, which is purged with CO_2 flow for 20 minutes. After this period, the experiment starts by applying a specified potential controlled by a potentiostat (SP-150, BioLogic). For all the catalysts, the applied potentials are: -1.7V, -1.6V, -1.5V, and -1.4V, which are corrected for the Ohmic drop

through a current interrupt (CI) measurement. Once the potential is adjusted, they are all converted to Reversible Hydrogen Electrode (RHE) using Equation 1.

$$E_{RHE}\,(V) = E_{Ag/AgCl}\,(V) + 0.059 \cdot pH + 0.206 \qquad \textit{Equation 1}$$

In each reaction, the experiment starts with linear scan voltammetry (LSV), with a scan rate of 10 mV/s from the open circuit potential (OCP) to the electrolysis potential, to study the kinetics of the reaction, identifying the onset potential (the potential at which the reaction starts), the overpotential, and the current density. The experiment starts with the LSV with a scan rate of 10 mV/s, and subsequently, when the applied potential is achieved, a chronoamperometric (CA) experiment is performed for one hour and forty minutes. The gas products formed during the electrocatalytic test in the cathode were subsequently analyzed with a gas chromatograph (GC) with two different capillary columns and two different detectors operating in online mode with injections at regular time intervals (22 minutes). The Pore-PLOT column with flame ionization detector (FID) was used to identify hydrocarbons and volatile organic compounds, and the Molesieve-5A column with the thermal conductivity detector (TCD) was used to characterize the hydrogen production. The liquid products from the electrolyte of the cathodic compartment were analyzed using nuclear magnetic resonance (NMR). To analyze these samples, an aliquot of 700µL was added to a sample tube, then 35µL of a standard of DMSO: D_2O and 35µL of D_2O were added.

The Faradic Efficiency (FE) for gas and liquid products is calculated following Equation 2 and Equation 3, respectively:

$$FE_{gas} = \frac{n \times V \times C \times F}{i \times V_M} \times 100 \qquad \textit{Equation 2}$$

$$FE_{liquid} = \frac{n \times V \times M \times F}{Q} \times 100 \qquad \textit{Equation 3}$$

n = number of electrons required in CO_2RR.
V = CO_2 gas flow rate (L/s) or volume of the electrolyte (L)
C = Volume fraction of the product detected by GC
V_M= Molar volume (22.4 L/mol)
F = Faraday constant (96485 C/mol)
i = average current (A)
M = molarity of the product (mol/L)
Q = total charge (C)

The working electrode (WE) contains the catalytic material; for this reason, is the only electrode that requires a previous preparation. In this case, carbon paper is used as a catalyst support due to its properties, such as electrical conductivity and porous structure. To deposit the catalyst onto the carbon paper surface, a catalyst ink is prepared based on the following procedures:

The ink for hybrid Cu_2O NCs and polymer catalyst without CNT (Figure 10a) is prepared by dispersing 2 mg of the catalytic material in 1 mL of ethanol, followed by sonication for 15-20 minutes. For the preparation of hybrid Cu_2O NCs ink with CNTs (Figure 10b) 2 mg of the catalytic material is dispersed in 1 mL of ethanol and then sonicated for 15-20 minutes. Separately, 2 mg of CNTs are dispersed in 950 µL of isopropanol in another vial and sonicated for 30 minutes. Then, 332 µL of the catalytic material solution is added to the CNTs solution and sonicated again for an additional 10-15 minutes.

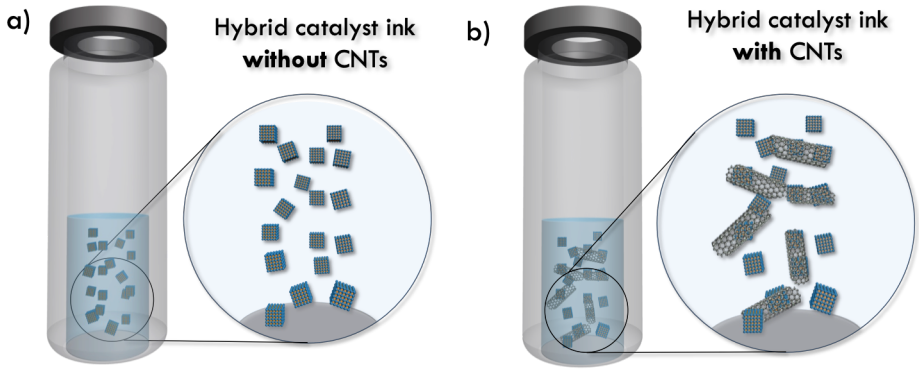

Figure 10. a) Hybrid catalyst ink without CNTs; b) Hybrid catalyst ink with CNTs.

For the preparation of the polymer catalyst ink with CNTs, 2 mg of the polymer and 2 mg of CNTs were mixed and grounded in the same vial. Then, the solution was dispersed in 1 mL of ethanol and sonicated for 15-20 minutes.

Once the catalyst ink is prepared, 25 µL is drop-cast onto Toray carbon paper (TGP-60, Alfa-Aesar), which has an area of 0.5 cm² (Figure 11). Considering that each side of the electrode is drop-cast with 12.5 µL, applying 12.5µL to each side of the electrode.

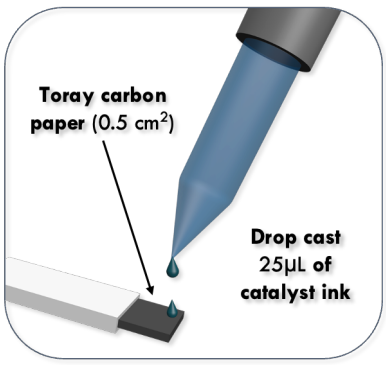

Figure 11.Drop-cast catalyst ink.

4. RESULTS & DISCUSSION

4.1 MATERIAL CHARACTERIZATION

4.1.1 Transmission Electron Microscopy (TEM)

Transmission Electron Microscopy (TEM) is an effective technique for characterizing nanomaterials such as oxide (Cu_2O) nanoparticles. It provides high-resolution imaging at the atomic or nanometer scale, making it well-suited for examining the size, shape, morphology, and crystallographic structures of Cu_2O nanoparticles. By means of an electron beam through a thin sample, TEM gives a detailed analysis of the nanoparticle morphology, crystalline structure, and lattice arrangement. This technique is essential for comprehending the physicochemical properties of Cu_2O nanoparticles, which directly affect their applications in catalysis.[16]

The characterized samples include the Cu_2O NCs and the hybrid catalysts. As shown in Figure 12, the cubic shape of the nanocubes is confirmed, and the dimensions of the cubes range from 70 to 100 nm.

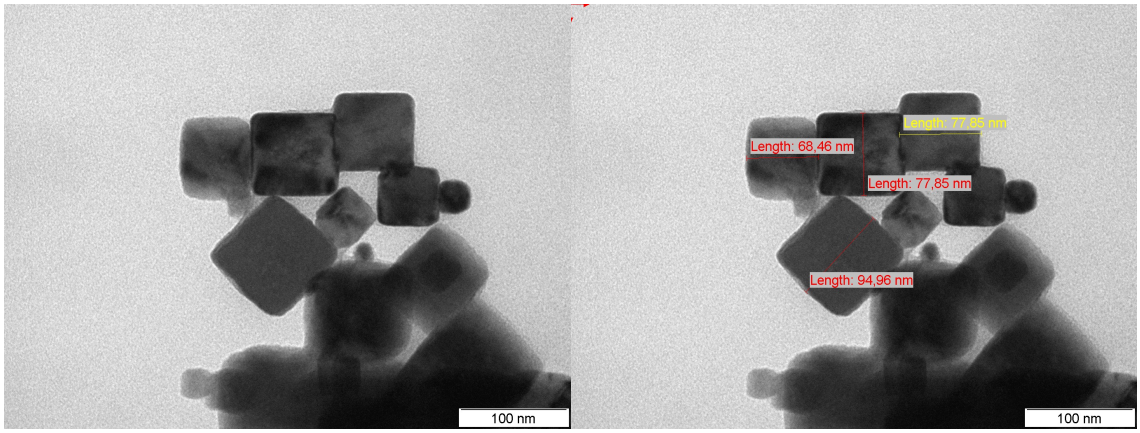

Figure 12. Cu_2O NCs TEM.

Figure 13a) and Figure 13b) represent Cu_2O@CoPc_2alk and Cu_2O@CoPc_3alk hybrid catalysts, respectively, showing the presence of a polymer layer covering the surface of the Cu_2O NCs, with a thickness ranging from 4 to 5 nanometers. Moreover, the cubic shape and size of the original particles remain intact during the click polymerization

reaction, with no evidence of structural degradation observed in the original Cu_2O NCs. These detailed results support the successful formation of a core-shell type system, achieved by using the CuAAC reaction, indicating effective surface functionalization without compromising the integrity of the core material.

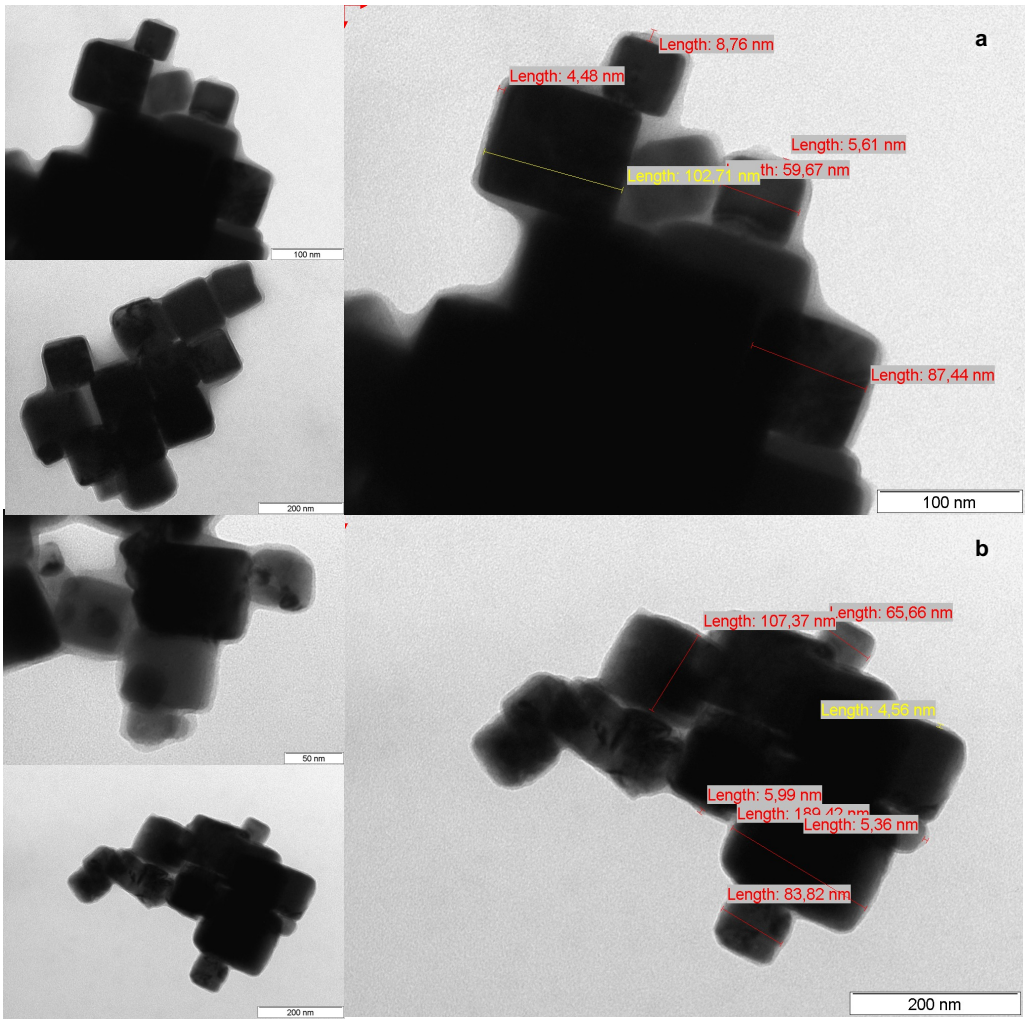

Figure 13. TEM images a) Cu_2O@CoPc_2alk; b) Cu_2O@CoPc_3alk.

4.1.2 High-resolution transmission electron microscopy and energy-dispersive X-ray spectroscopy (HRTEM-EDS)

High-resolution transmission electron microscopy (HRTEM) and energy-dispersive X-ray spectroscopy (EDS) are powerful techniques used to analyze structural characteristics and elemental composition of nanoparticles in detail.

The elemental composition of the hybrid catalysts includes carbon (C), nitrogen (N), and cobalt (Co) from the polymer layer, along with copper from the Cu_2O NCs. This configuration enables a clear distinction between the core and shell components of the system. The EDS mappings of Cu_2O@CoPc_2alk and Cu_2O@CoPc_3alk are shown in Figures 14a and 14b, respectively. In Figure 14a, the mappings reveal a uniform distribution of C, N, and Co over the Cu_2O NCs and the thin polymer layer surrounding them. Copper is evenly distributed throughout the core, confirming that it is composed of Cu_2O. The elemental maps for Co and N also exhibit uniform distributions, indicating complete coverage of the nanocubes by the polymer. In the overlay image, the polymer layer appears primarily composed of carbon, which is the dominant element in the polymer matrix, along with detectable amounts of Co and N coating the nanocubes. Analogously, in Figure 14b, the Cu_2O@CoPc_3alk sample shows comparable elemental distributions of Co, N, and C, although the polymer layer in this case appears thicker.

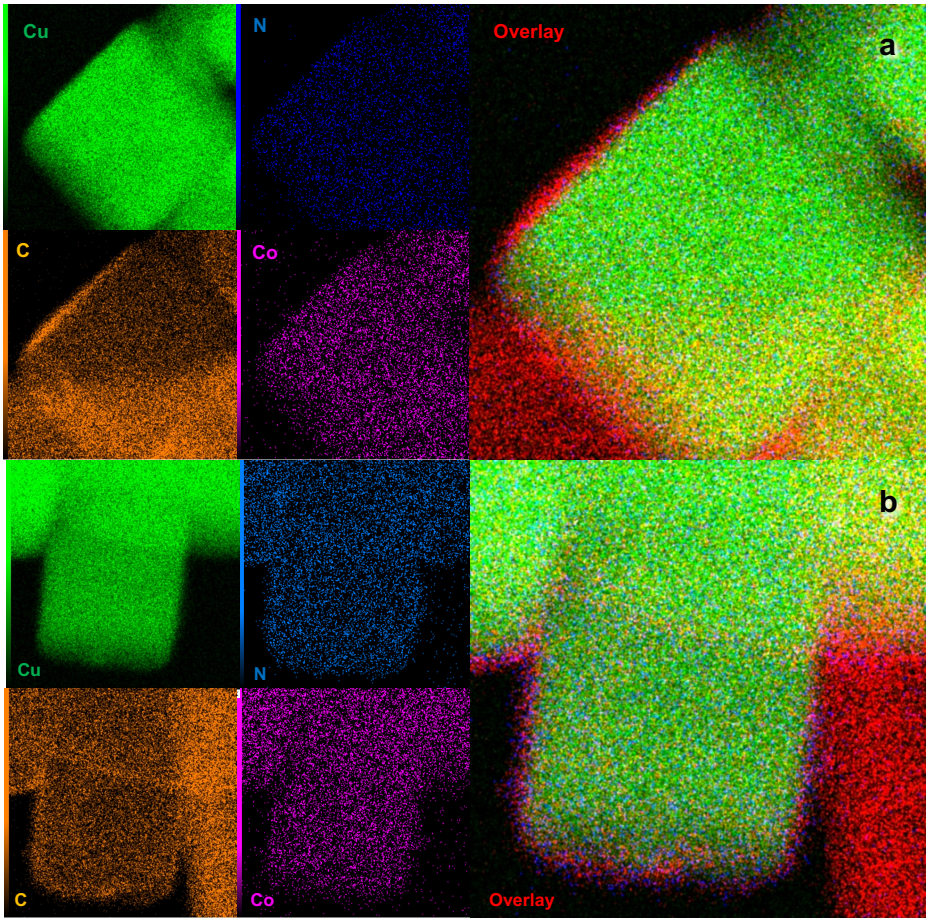

Figure 14. EDS mapping: a) Cu_2O@CoPc_2alk; b) Cu_2O@CoPc_3alk.

4.1.3 Attenuated total reflectance - Fourier transform infrared spectroscopy (ATR-FTIR)

Infrared spectroscopy provides chemical and structural insights through molecular analysis by identifying functional groups that have unique vibrational frequencies in the infrared spectrum, particularly within the mid-range (4000–400cm^{-1}).[17]

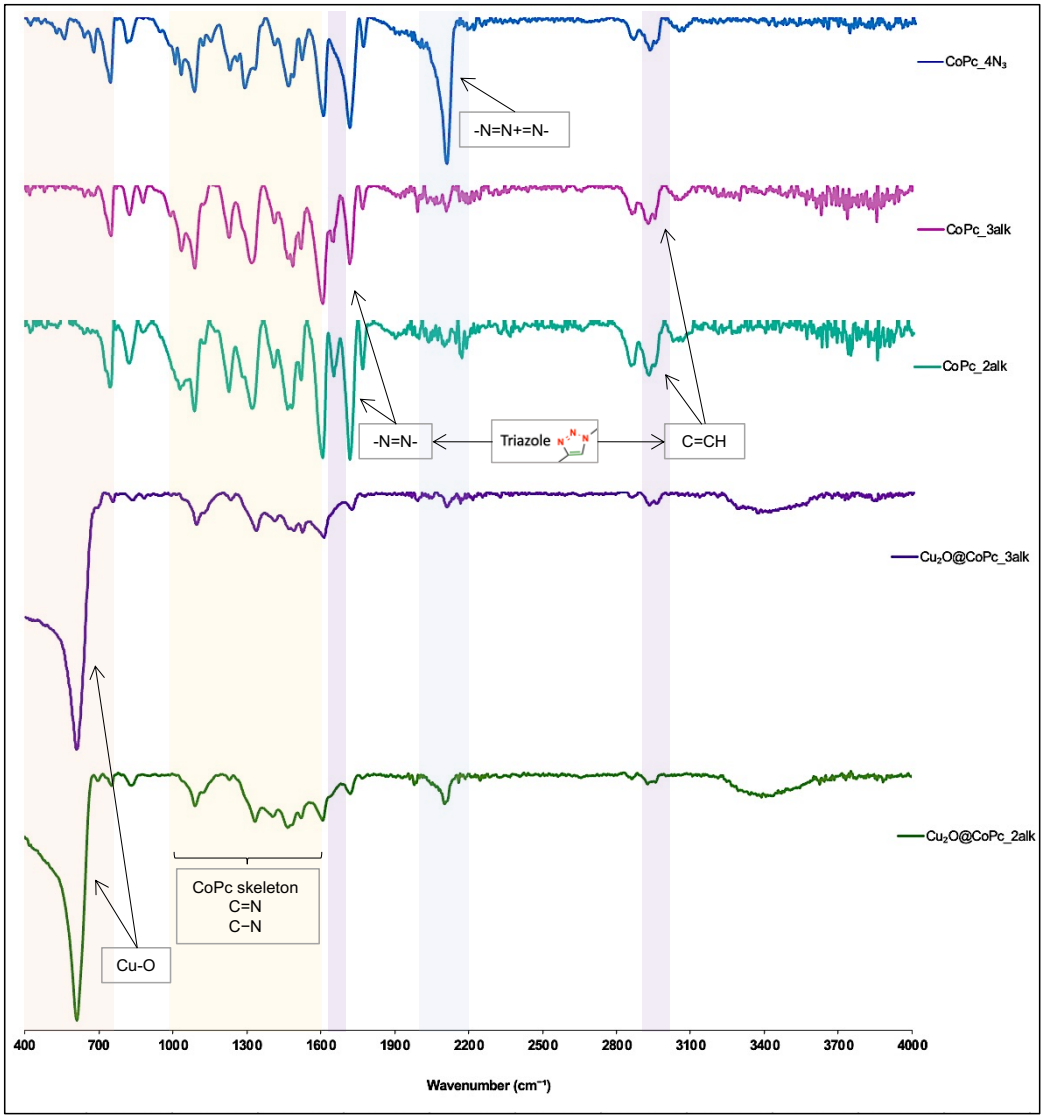

Figure 15. ATR-FTIR of the catalysts.

Figure 15, displays the spectra of all the catalysts studied in this work. The hybrid Cu_2O NCs, Cu_2O@CoPc_2alk and Cu_2O@CoPc_3alk, the purple and green spectra,

respectively, show a peak at 600 cm^{-1} attributed to the Cu-O stretching from the Cu_2O NCs. Moreover, in the CoPc_$4N_3$ spectra, represented in blue, a distinct peak appears at 2100 cm^{-1} which corresponds to the azide group ($-N=N^+=N^-$) of the monomer cobalt (II) tetrazidophthalocyanine.[14,18] In contrast, this peak is absent in the other spectra, suggesting the polymer formation. However, in the Cu_2O@CoPc_2alk, a minor peak is present in this region, which might be ascribable to unreacted monomer molecules persistent in the hybrid catalyst. Additionally, the appearance of the N=N stretching band at 1650 cm^{-1} and the C=CH stretching band at 2900 cm^{-1}, both associated with triazole rings, indicate the successful formation of the polymeric matrix.[14,19]

In all the spectra, there are prominent peaks from 1000 cm^{-1} to 1600 $cm^{-1,}$ which serve as evidence for the presence of the C=N and C−N bands associated with the skeletal vibrations of the phthalocyanine rings from cobalt (II) tetraminophthalocyanine. [20] Subsequently, these results confirm the successful formation of the CoPc-based polymers (CoPc_2Alk and CoPc_3Alk) and their effective incorporation onto the Cu_2O NCs surface by following the templated-CuAAC reaction.

4.1.4 Powder X-ray diffraction (PXRD)

The synthesized Cu_2O NCs and hybrid materials were characterized by powder X-ray diffraction (PXRD). XRD is a non-destructive material analysis technique commonly utilized in materials science to determine and characterize crystalline phases of powdered materials. Through the determination of diffracted X-ray intensities and angles, XRD gives valuable information regarding atomic order, lattice parameters, and overall crystallinity of the sample, thus enabling accurate structural analysis of formed nanoparticles.[21]

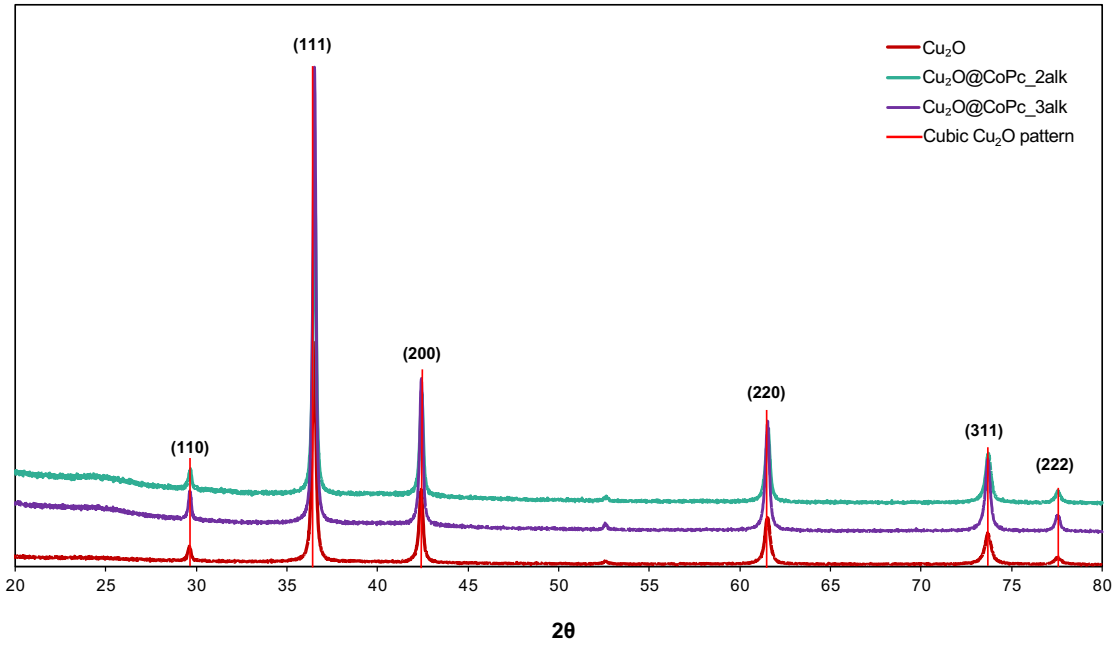

Figure 16. XRD hybrid materials.

In Figure 16 the cubic Cu_2O pattern, the red, is used as a reference diffraction pattern for the hybrid materials, in which all six strong and well-defined peaks are well matched, which were found at 2θ positions of approximately 29.6°, 36.5°, 42.4°, 61.5°, 73.7°, and 77.5°, corresponding to the (110), (111), (200), (220), (311), and (222) crystallographic plans, respectively, of the facets of Cu_2O.[15]

The peak sharpness indicates a high level of crystallinity in the sample, validating the development of the desired Cu_2O crystal phase.[22] Moreover, the amorphous phase of the polymers is not reflected in the spectra; all these results suggest that the crystalline structure does not change after the click polymerization.

4.1.5 Determination of surface electrochemical active sites of cobalt phthalocyanine in polymer

To assess the surface concentration of electroactive cobalt phthalocyanine units in the polymers CoPc_2alk and CoPc_3alk, cyclic voltammetry tests are conducted in Ar-saturated 0.1M $KHCO_3$ at scan rates ranging from 10 to 60 mV·s-1. As shown in Figure 17.

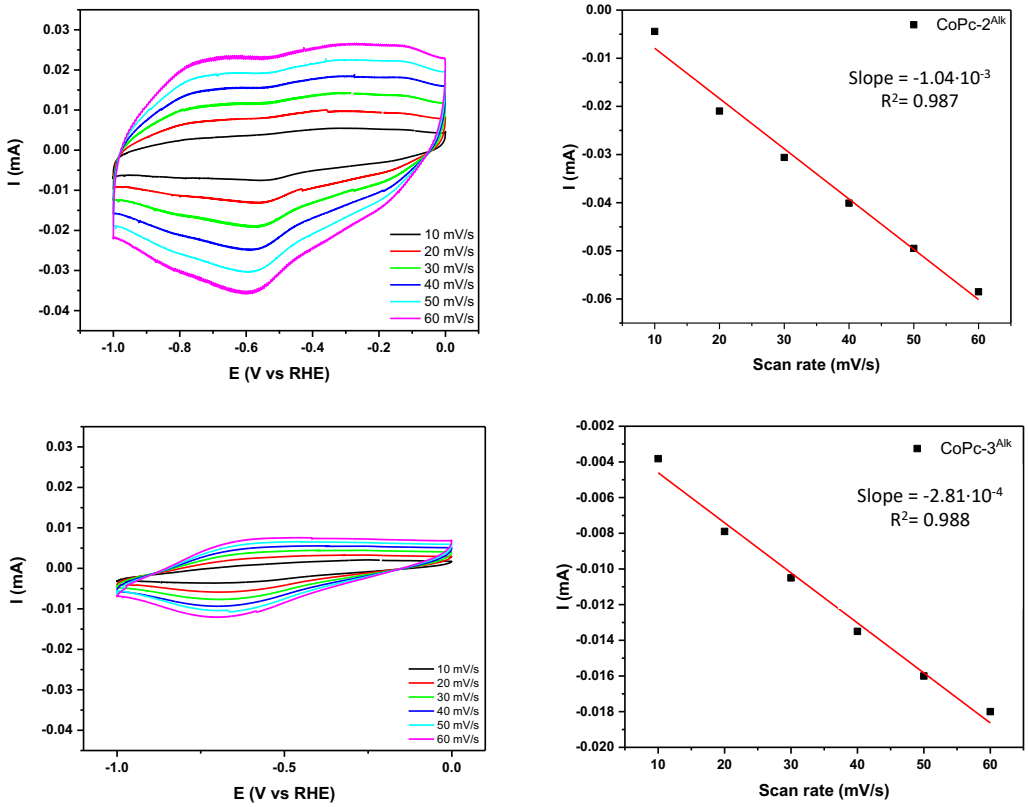

Figure 17. Cyclic voltammetry and linear regression of the polymers at the applied scan rates.

The surface coverage (T_0) is calculated using is calculated using the Equation 4, where "n" represents the number of electrons involved, which here is 1 electron; "F" denotes the Faraday constant (96485,3321 C/mol); "A" indicates the geometrical surface area of the electrode (0,5 cm^2); "R" is the gas constant (8,314 J/mol·K); and "T" is the temperature during the test (298K).[23]

$$\text{slope} = n^2F^2A\Gamma_0/4RTA \qquad \textit{Equation 4}$$

With the CoPc_2alk, the electrochemical surface of cobalt phthalocyanine is 2,1425 nmol/cm^2, while in the CoPc_3alk, it is 0,59736 nmol/cm^2. These values indicate a higher electroactive area for the CoPc_2alk.

4.1.6 UV-Vis spectroscopy (UV-Vis)

UV-Vis spectroscopy involves the excitation of atom's outermost electrons, which are responsible for chemical bonding in the formation of molecules. When electromagnetic radiation in the ultraviolet (UV) or visible range is absorbed, electronic transitions between energy levels occur, giving rise to absorption bands in the UV-Vis spectrum. These transitions take place when the energy of the incident radiation matches the energy difference (or gap) between two electronic states, allowing an electron to be promoted from a lower to a higher energy level. [24]

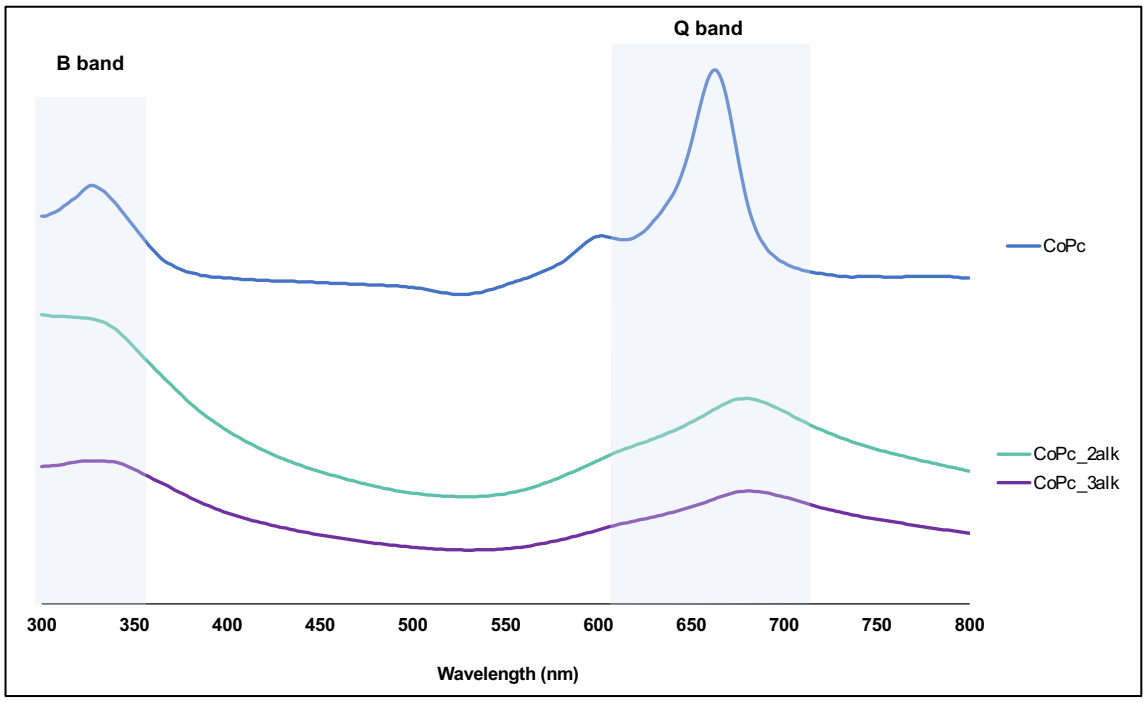

Figure 18.UV-Vis spectra of the polymeric materials.

Figure 18. shows the UV-Vis spectra of the polymeric materials dissolved in DMF, the concentration was $2.4 \cdot 10^{-2}$ mg/mL for all of them. The CoPc spectra usually display characteristic absorbance bands: the Q band and the Soret band, shown in the frontier molecular orbital diagram in Figure 19. The Q band, ranges from 600 to 700 nm, that corresponds with the $a_{1u}(\pi)$-$e_g(\pi^*)$ transition from the highest occupied molecular orbital (HOMO) to the lowest unoccupied molecular orbital (LUMO). The B band (Soret band) is placed at 300–350 nm because of the deeper $a_{2u}(\pi)$ to LUMO transition.[9]

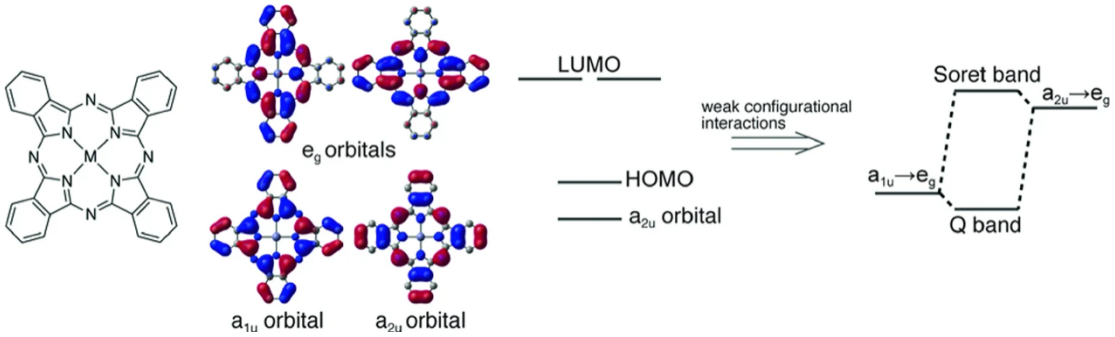

Figure 19. Frontier molecular orbital diagrams of metal phthalocyanine.[25]

The Q bands of the polymeric materials CoPc_2alk and CoPc_3alk are slightly red-shifted compared to the Q band of the CoPc monomer. This broadening of the Q band is mainly due to changes in molecular symmetry and increased delocalization of π-electrons across the extended conjugated framework. In the monomeric CoPc, electron delocalization is mostly confined within the highly symmetric macrocyclic core, resulting in well-defined electronic transitions and sharp absorption peaks. However, polymerization reduces the symmetry in the polymeric forms, and the addition of alkyl substituents allows π-conjugation to extend over multiple phthalocyanine units, altering the electronic environment and affecting the distribution of electronic transition energies throughout the polymer chain. [9,25,26]

4.1.7 X-ray Photoelectron Spectroscopy (XPS)

X-ray Photoelectron Spectroscopy (XPS) is a widely used surface analytical technique that provides quantitative and qualitative information about the chemical state of the elements present on the material surface. Through the analysis of core-level electron binding energies, XPS enables the precise determination of the elemental surface composition as well as the oxidation states of the various constituent elements. This approach provides determining insights into the surface chemistry and electronic structure of materials that are crucial for understanding their physicochemical properties and operational performances.[27]

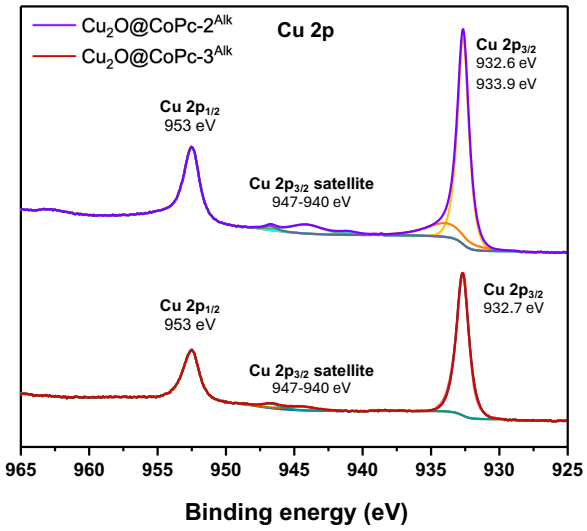

Figure 20.Cu 2p XPS analysis in the hybrid catalysts.

Figure 20, displays the Cu 2p XPS analysis in the hybrid catalysts. The Cu_2O@CoPc_2alk, the purple spectra, show two peaks attributed to Cu^+ at 932.6 eV and 953 eV, along with one peak for Cu^{2+} at 933.9 eV. Moreover, in the region of 947-940 eV, there are satellite peaks corresponding to Cu^{2+} and Cu^+. [28] The traces of Cu^{2+} on the catalytic surface can be linked to Cu^+ oxidized to Cu^{2+} due to the unavoidable exposure of the sample to air. Moreover, in the case of Cu_2O@CoPc_3alk, as shown by the red spectra, the two peaks at 932.7 eV and 953 eV correspond to Cu^+, and the satellite peaks in the region of 947-940 eV are consistent with those observed for Cu_2O@CoPc_2Alk.

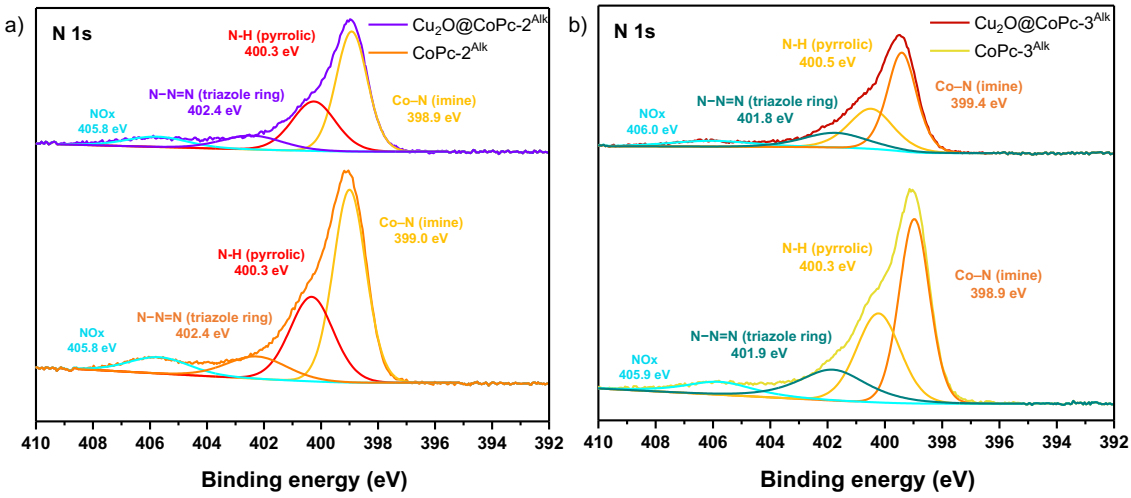

Figure 21. XPS spectra of N 1s. a) Cu_2O@CoPc_2Alk and CoPc_2Alk; b) Cu_2O@CoPc_3Alk and CoPc_3Alk.

Figure 21, provides the XPS spectra of N 1s over the surfaces of the hybrid and polymer catalysts. Figure 21a) represents the catalysts with the 2alk morphology, and Figure 21b) illustrates the 3alk morphology. Firstly, in both figures, the Co-N imine band is observed above 399-398 eV, typically attributed to cobalt (II) phthalocyanine. Secondly, XPS spectra for all the samples show a peak between 400.3-400.5 eV, which is attributed to pyrolytic N groups. Moreover, there is also evidence of the triazole ring according to the signals at 402.4 eV in Cu_2O@CoPc_2alk and CoPc_2alk, at 401.8 eV in Cu_2O@CoPc_3alk, and at 401.9 eV in CoPc_3alk, which are indicative of the N-N=N bonds from the triazole ring. [29–31] Finally, a weaker band appears in all spectra between 405.8 eV and 406.0 eV, related to nitrogen oxides (NOx).[31]

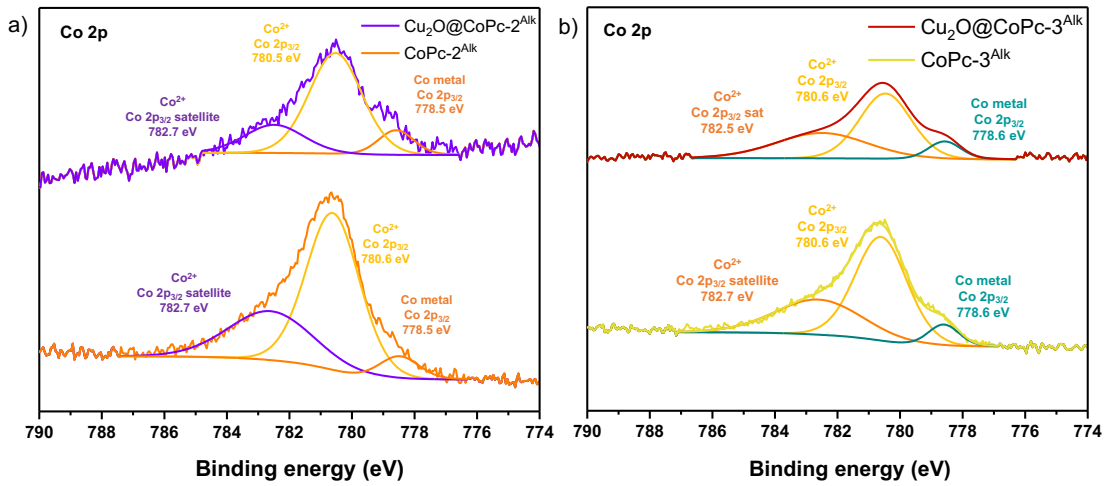

Figure 22. Co 2p XPS. a) Cu_2O@CoPc_2Alk and CoPc_2Alk; b) Cu_2O@CoPc_3Alk and CoPc_3Alk.

Figure 22 displays the Co 2p XPS analysis for all the catalysts. On one hand, Figure 22a shows the catalysts exhibiting the 2alk morphology (Cu_2O@CoPc_2Alk and CoPc_2Alk), where the peaks between 780.5-780.6 eV correspond to Co $2p_{3/2}$ of Co^{2+}, along with the satellite peaks at 782.7 eV in both spectra. Additionally, there is a peak at 778.5 eV assigned to Co $2p_{3/2}$ of metallic Co, typically attributed to CoPc systems. [31,32] On the other hand, for the catalysts exhibiting 3alk morphology (Cu_2O@CoPc_3Alk and CoPc_3Alk) in Figure 22b, the Co $2p_{3/2}$ of Co^{2+} appears at 780.6 eV in both spectra, with the corresponding satellite peaks around 782.5 eV-782.7. Moreover, the metallic Co peak, at 780.5-780.6 eV, is also visible in these samples. Notably, these spectral features closely resemble those observed for the Cu_2O@CoPc_2Alk and CoPc_2Alk, indicating similar chemical states and electronic environments.[31,32]

5. ELECTROCHEMICAL TESTS

To evaluate the influence of the spatial distribution and the dispersion of the catalyst in tandem catalysis, all the catalysts were tested with and without the CNTs. Firstly, the Cu_2O NCs were tested independently as a reference material to provide a comparison point for the hybrid materials. Separately, the polymers were also tested to determine the electrochemical performance of these materials under CO_2. Since the polymers serves as a CO-selective component in the hybrid catalytic system, these tests were essential to evaluate several key aspects: (i) their intrinsic activity as CO_2-to-CO catalyst, (ii) the on-set potential for CO generation specific to each polymer, and (iii) a comparative analysis of their overall performance.

5.1 LSV RESULTS

LSV experiments have been conducted to determine the onset potential, overpotential, and current density.

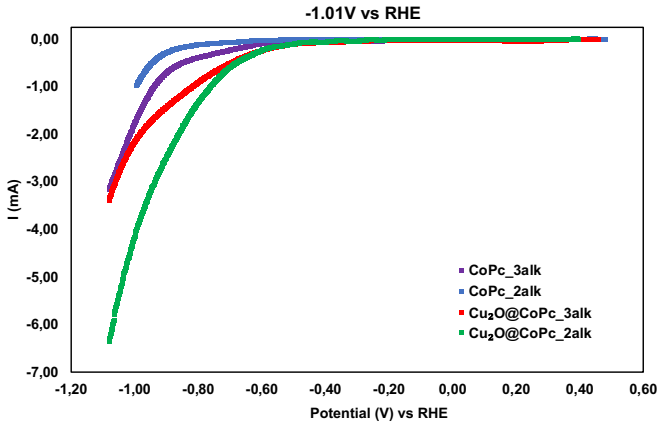

Figure 23. LSV at -1.01V_{RHE}.

In Figure 23, the linear scan voltammetry (LSV) curves at -1.01V_{RHE} of both the polymers and the corresponding hybrid materials are presented. It is observed that the current densities associated with the pure polymer samples are higher than those of the hybrids. This indicates that the overall electrochemical activity under the tested conditions is lower in the hybrid materials. As a result, the onset potential, defined as the potential at which the CO_2RR initiates, appears at more negative values in the polymeric materials.

5.2 FE (%) RESULTS

5.2.1 Cu_2O NCs

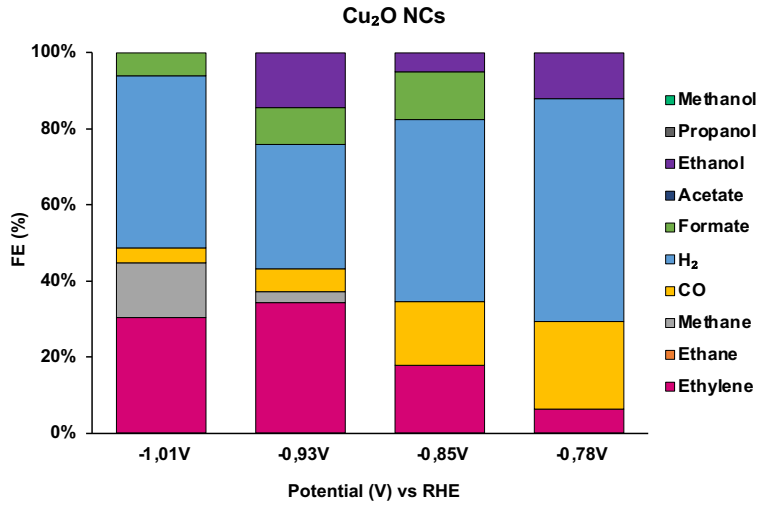

Figure 24. Cu_2O NCs FE (%) at various applied potentials (V) vs RHE.

The Cu_2O NCs were evaluated at four different applied potentials: –1.0 V, –0.93 V, –0.85 V, and –0.78 V vs RHE. Figure 24 shows the Cu_2O NCs' FE% at each applied potential. The findings indicate that both C_1 and C_2 products are generated, with no clear selectivity for any specific product. Methane, carbon monoxide, and formate are produced in smaller amounts, while hydrogen (41.6%) and ethylene (27.9%) are the primary products at –1.0 V vs RHE, the highest potential tested. At –0.93 V vs RHE, ethylene remains the dominant hydrocarbon product, while hydrogen production decreases slightly to 32.4%. Notably, ethanol emerges as a detectable product with a Faradaic efficiency of 14.3%, methane, carbon monoxide, and formate are also present, though in relatively minor amounts. At –0.85 V vs RHE, HER becomes the main reaction pathway, resulting in a significant reduction in hydrocarbon production. This trend continues at –0.78 V vs RHE, although a noticeable increase in carbon monoxide production is observed.

Despite this notable rise in CO concentration at lower potentials, it suggests that the CO intermediate may desorb from the catalyst surface before it can be further reduced to one-carbon or multi-carbon products. This behavior implies that the binding strength of CO

to the Cu surface centers decreases with the decreasing potential, hindering its further transformation into more reduced species.

5.2.2 Polymers

The polymers are specifically designed to produce CO as the main product. To assess their catalytic efficiency, both polymers underwent testing at four distinct applied potentials relative to the RHE.

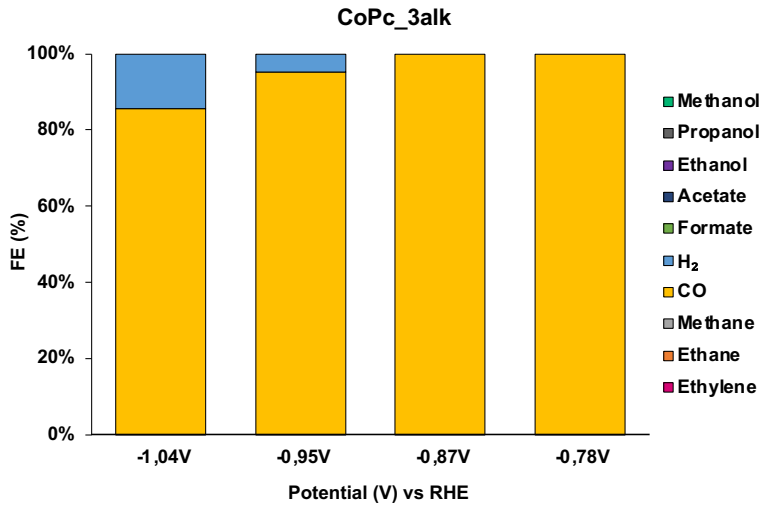

Figure 25. CoPc_3alk FE (%) at various applied potentials (V) vs RHE.

As illustrated in Figure 25, the CoPc_3alk polymer catalyst shows strong selectivity for CO generation. At applied potentials of -0.78 V and -0.87 V vs RHE, the catalyst achieves complete CO production with no detectable hydrogen evolution. When the potential is set at -0.95 V, CO selectivity slightly decreases to 94.29%, paired with 5.71% hydrogen production. Increasing the potential to -1.04 V leads to an 85.65% CO selectivity, with higher hydrogen, indicating a rise in competition from hydrogen production as potentials become more negative. Overall, CoPc_3alk still exhibits excellent CO selectivity across the explored applied potentials.

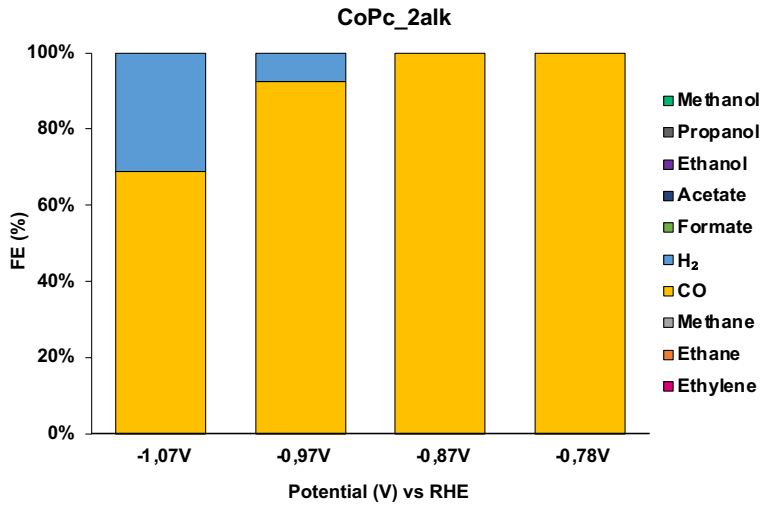

Figure 26. CoPc_2alk FE (%) at various applied potentials (V) vs RHE.

In contrast, Figure 26 demonstrates that CoPc_2alk follows a similar pattern, though with slightly diminished performance at higher overpotentials. At -0.78 V and -0.87 V, CO selectivity remains at 100%, such as CoPc_3alk. However, at -0.97 V, the CO selectivity declines to 91.04%, with an increase in hydrogen production. At -1.07 V, the CO selectivity further drops to 68.39%, while hydrogen production rises to 30.93%. The small difference observed in CO and H_2 production between CoPc_2Alk and CoPc_3Alk is attributed to the applied potential, which are slightly more negative for CoPc_2Alk.

In general, both systems exhibit excellent performance for the electrochemical CO_2RR, achieving selective CO production at low overpotentials. At more negative potentials, syngas (CO:H_2) formation is favored, with CO remaining the predominant product.

5.2.3 Polymers with CNTs

To enhance the catalytic efficiency and selectivity of polymer systems, their performance was examined when mixed with CNTs. CNTs act as conductive supports that improve the dispersion of the polymer catalyst while minimizing unwanted π–π stacking interactions, which often restrict access to active sites. This strategy focuses on optimizing the electrocatalytic performances for CO_2 reduction.

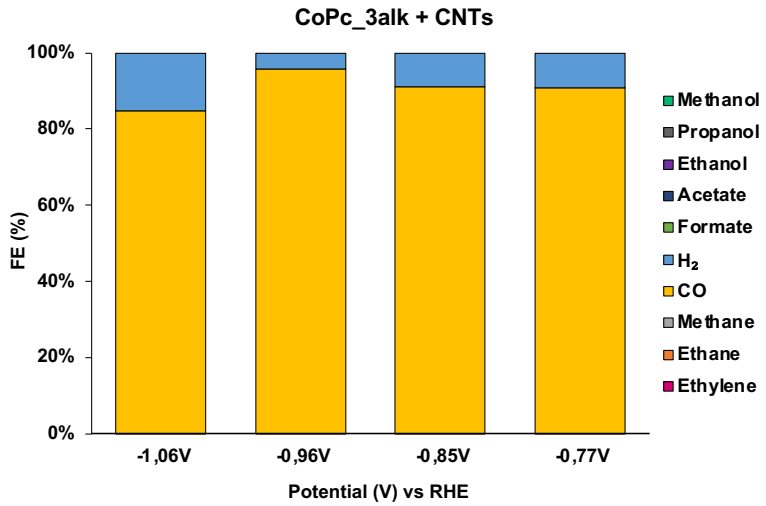

Figure 27. CoPc_3alk + CNTs FE (%) at various applied potentials (V) vs RHE.

The performance results for CoPc_3alk mixed with CNTs (Figure 27) were not as expected. Notably, at lower applied potentials, CO selectivity decreases, and at higher potentials, there was no substantial improvement. At -1.06 V, CO selectivity reached 82.47%. At -0.96 V, CO selectivity increased to 98.48%, small amounts of hydrogen. At -0.85 V and -0.77 V, CO production remained relatively high at 92.89% and 92.34%, respectively, reflecting a slight decrease in CO selectivity compared to the polymer without CNTs.

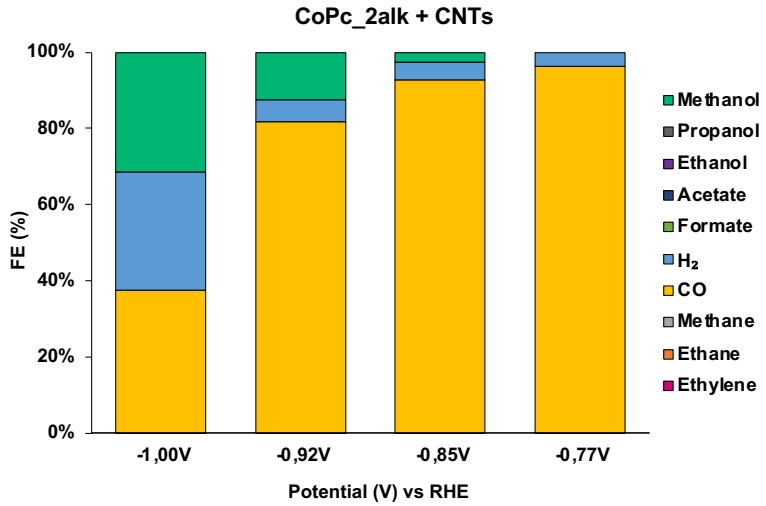

Figure 28. CoPc_2alk + CNTs FE (%) at various applied potentials (V) vs RHE.

Conversely, Figure 28 illustrates that CoPc_2alk with CNT produced methanol, which is particularly noteworthy. This finding suggests that the structural differences and dispersion characteristics of the polymer on CNTs can significantly affect product distribution. At -1.00 V, the composite yielded 38.10% CO, 31.63% hydrogen, and 31.88% methanol. At -0.92 V, CO selectivity increased to 82.31%, with 12.44% methanol and 5.82% hydrogen. At -0.85 V, the results showed 93.15% CO, 2.71% methanol, and 4.69% hydrogen. At -0.77 V, the catalyst achieved 96.18% CO with 3.80% hydrogen and no methanol was detected.

These results reveal a noticeable trend, the methanol formation increases at higher overpotentials, while CO selectivity improves at lower overpotentials. The methanol formation could be attributed to the better dispersion and less aggregation of the CoPc moieties of the CoPc_2Alk, where the intermolecular pi-pi staking interactions are minimized, favoring the further *CO reduction and protonation to methanol, which is released to within the stern layer, as is proposed in Figure 29.[33] This behavior emphasizes the significant effect of polymer structure and support interaction on catalytic selectivity.

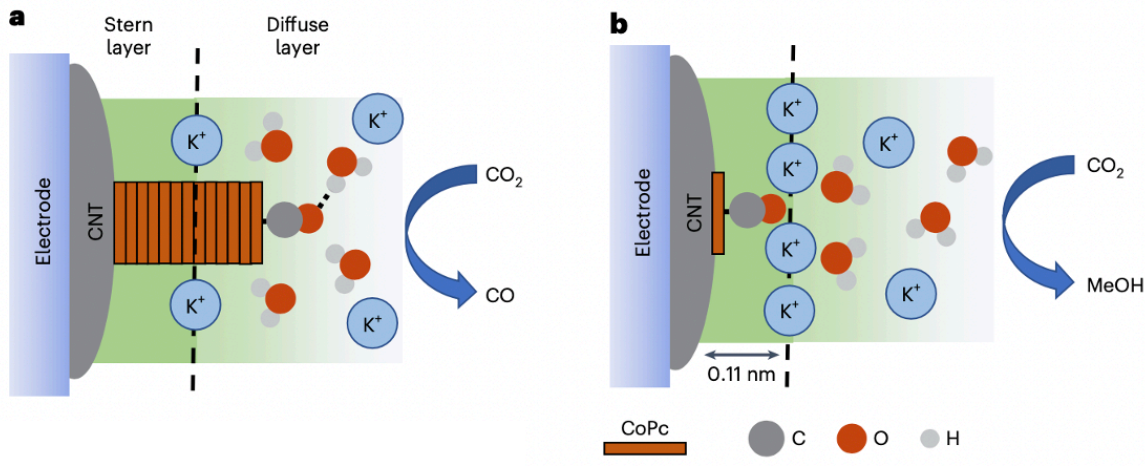

Figure 29. Proposed scheme of interfacial structures with and without CoPc aggregates. [33]

5.2.4 Hybrid materials

The hybrid materials are expected to produce multicarbon products, with higher selectivity than the Cu_2O NCs.

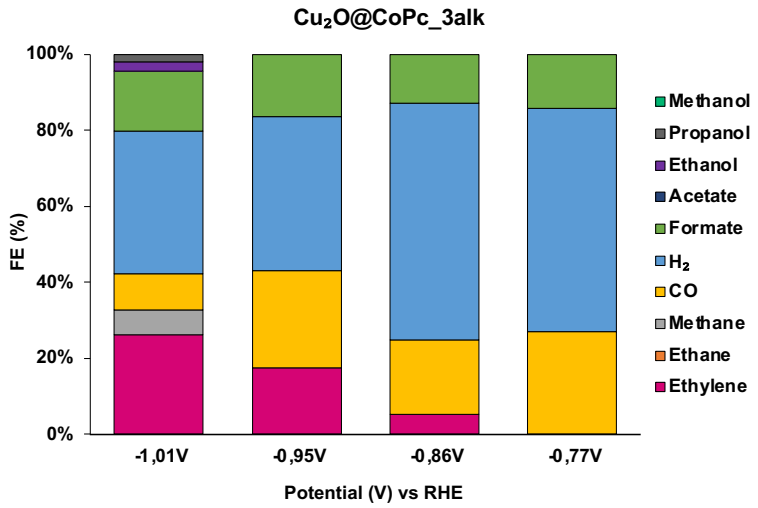

Figure 30. Cu_2O@CoPc_3alk FE (%) at various applied potentials (V) vs RHE.

Figure 30 shows the FE% of the Cu_2O@CoPc_3alk hybrid for CO_2 reduction at different applied potentials. At -1.01 V_{RHE}, the catalyst produces a wide variety of products, ethylene is the main C_2 product with a FE of 26.11%, CO is formed at 9.64%, hydrogen evolution is significant at 37.64% and methane is present in lower amounts. Additionally, formate reaches 15.78%, with smaller amounts of ethanol and propanol, indicating the formation of C_1 to C_3 products at this potential. At -0.95 V_{RHE}, the product distribution changes noticeably, ethylene remains present at 17.59%, whereas methane and higher alcohols are no longer detected, CO production increases to 25.57%, hydrogen becomes the dominant product at 40.82% and formate production remains steady, suggesting a shift toward simpler C_1 and C_2 products. At -0.86 V_{RHE}, the trend continues with further reduction in multi-carbon products; ethylene drops to 5.23%, CO rises to 19.25%, hydrogen dominates at 61.65%, formate production slightly decreases, and no higher-order products are observed. Finally, at -0.77 V_{RHE}, only C_1 products are present, CO reaches 27.60%, hydrogen is the main product at 60.16%, and formate remains steady. No ethylene, methane, or alcohols are detected at this potential.

These findings suggest that the formation of multi-carbon products becomes more favorable at higher overpotentials, while lower overpotentials favor simpler C_1 species and promote hydrogen production.

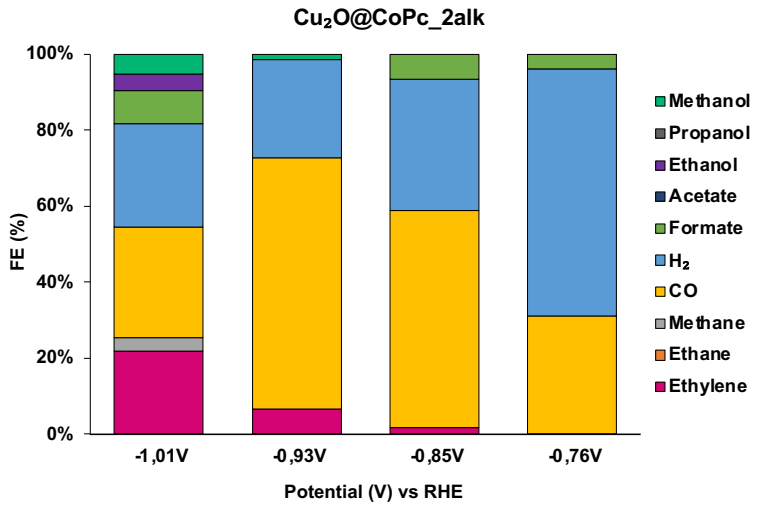

Figure 31. Cu_2O@CoPc_2alk FE (%) at various applied potentials (V) vs RHE.

Figure 31 displays the Cu_2O@CoPc_2alk hybrid FE% results at various applied potentials. At -1.01 V_{RHE}, the system produces both C_1 and C_2 products, with limited formation of multi-carbon compounds, ethylene is generated at 23.37%, while methane appears at minor amounts, CO is the major product at 30.98%, and hydrogen evolution is also significant at 29.23%. Moreover, formate reaches 9.17%, with smaller amounts of ethanol and methanol, indicating some C_{2+} selectivity at this potential. At -0.93 V_{RHE}, the product distribution shifts notably, ethylene drops to 6.66%, and methane and ethanol are no longer detected. CO remains as the dominant product, hydrogen decreases to 26.34%, and methanol is still present but with a minor FE. At -0.85 V_{RHE}, ethylene is nearly eliminated, while CO production remains high at 61.01%, hydrogen production increases to 36.87%, and formate appears at 7.20%, while methanol and other alcohols are no longer seen. At the least negative potential of -0.76 V_{RHE}, only C_1 products are observed, CO is produced at 31.49%, hydrogen evolution is dominant at 65.85%, and formate stays with lower FE (%), there's no ethylene or alcohols formed under these conditions. These findings suggest that the formation of multi-carbon products in Cu_2O@CoPc_2alk is favored at

higher overpotentials, while hydrogen evolution becomes more dominant as the potential becomes less negative.

In. general, both hybrid systems promote C_{2+} product formation at higher overpotentials. However, Cu_2O@CoPc_3alk exhibits a broader product range, including C_3 compounds like propanol, indicating greater catalytic complexity. Notably, hydrogen production is more prominent in the Cu_2O@CoPc_3alk system, pointing to stronger competition between HER and CO_2RR. Which means that the CO_2RR efficiency is higher in Cu_2O@CoPc_2alk than in Cu_2O@CoPc_3alk.

5.2.5 Hybrid materials with CNTs

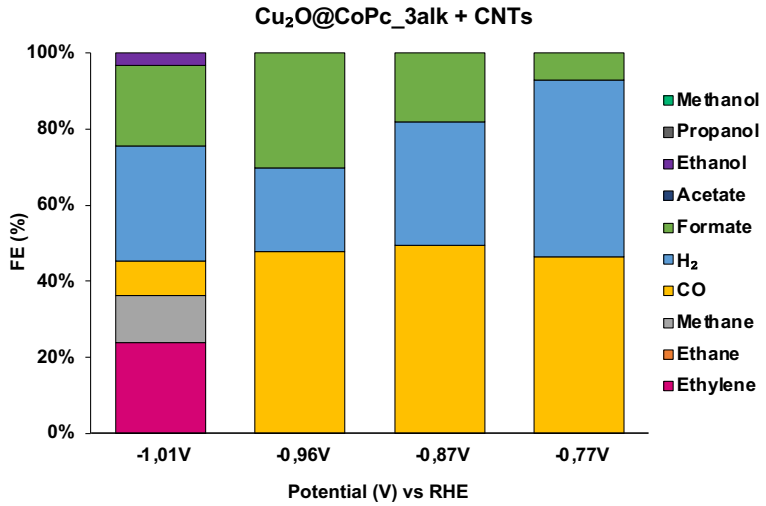

Figure 32. Cu_2O@CoPc_3alk + CNTs FE (%) at various applied potentials (V) vs RHE.

Figure 32 displays the FE% of the hybrid material Cu_2O@CoPc_3alk mixed with carbon nanotubes. At -1.01 V_{RHE}, the system shows a broad product distribution, including multi-carbon compounds. Ethylene was produced with a FE of 25.42%, and methane was also detected up to 12.96%. The selectivity toward CO was relatively low at this potential, reaching only 9.50%, while hydrogen evolution was significantly detected. Additionally, 22.55% of formate and a small amount of ethanol were produced; no other products such as ethylene, propanol, acetate, or methanol were observed. At -0.96 V_{RHE}, the product distribution shifts notably, where ethylene and methane are no longer detected, and CO

production increases to 51.04%, becoming the dominant product. Hydrogen evolution decreases, but it remains in a considerable amount, while formate production increases slightly to 32.35%. At -0.87 V_{RHE}, CO production remains high at 52.04%, indicating selectivity for CO at this intermediate potential, hydrogen formation also rises to 33.98%, and formate decreases slightly. No C_{2+} products or alcohol products are observed, suggesting a reduction in multi-carbon product formation at this less negative potential. Finally, at -0.77 V_{RHE}, the lowest potential tested, CO production drops to 44.78%, while hydrogen evolution becomes the dominant pathway with a FE of 45.04%. Formate is still present but with minor amounts, and no other CO_2 reduction products are detected.

Overall, the data show that CO production is most favorable at intermediate potentials (-0.96 V and -0.87 V), while multi-carbon products such as ethylene, methane, and ethanol are only formed at more negative potentials (-1.01 V). Hydrogen evolution becomes increasingly competitive at lower overpotentials, especially at -0.77 V, where it surpasses CO production.

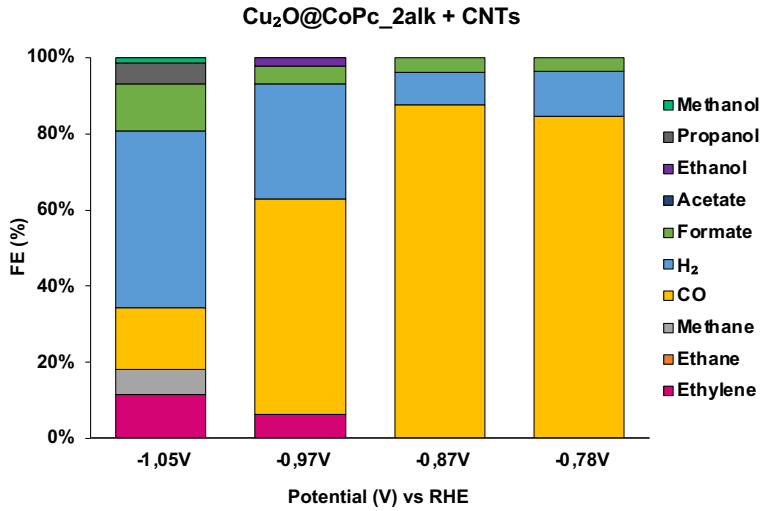

Figure 33. Cu_2O@CoPc_2alk + CNTs FE (%) at various applied potentials (V) vs RHE.

Figure 33 shows the FE distribution of the hybrid material Cu_2O@CoPc_2alk mixed with CNTs. Multi-carbon products were only detected at the most negative potential of -1.05 V_{RHE}, where ethylene, methane, propanol, methanol, and formate were formed, along with CO and a dominant hydrogen production of 48.54%. As the potential was stepped

to -0.97 V_{RHE}, CO production significantly increased to 59.10%, while HER activity decreased to 31.33%, and only minor amounts of ethylene and ethanol were detected. At -0.87 V_{RHE}, the system showed excellent selectivity toward CO of 94.52%, with minimal hydrogen and formate formation, and no other multi-carbon products were detected. Similarly, at -0.78 V_{RHE}, CO remained high, reaching 90.25% of FE, with a slight increase in hydrogen production to 12.62% and a small amount of formate. These results suggest that CO formation is strongly favored at moderate potentials, while more negative potentials are needed to produce C_{2+} products and alcohols.

When comparing hybrid materials with and without CNTs, a clear difference in product distribution appears. The addition of CNTs significantly increases CO production and reduces hydrogen production, especially at intermediate potentials where faradaic efficiencies are higher. However, contrary to expectations, the formation of C_{2+} products such as ethylene, ethanol, and propanol does not improve with CNT addition; instead, these multi-carbon products are mainly suppressed.

Furthermore, comparing the two hybrid systems (Cu_2O@CoPc_2alk and Cu_2O@CoPc_3alk) reveals similar product distributions. At lower overpotentials, CO is the main product along with hydrogen evolution and trace amounts of formate. In contrast, at more negative overpotentials, multi-carbon product formation is encouraged, still alongside hydrogen production. A key difference is in overall CO_2 reduction efficiency, with the Cu_2O@CoPc_2Alk system showing higher Faradaic efficiencies for CO_2 reduction products compared to Cu_2O@CoPc_3Alk, indicating greater catalytic effectiveness.

5.2.6 Control experiment CoPc_2alk/Cu_2O NCs

Control experiment was conducted by physical mixture of the CoPc_2Alk polymer and Cu_2O NCs in a 1:1 weight ratio, to evaluate whether the two components can function independently and potentially cooperate in C–C coupling reactions.

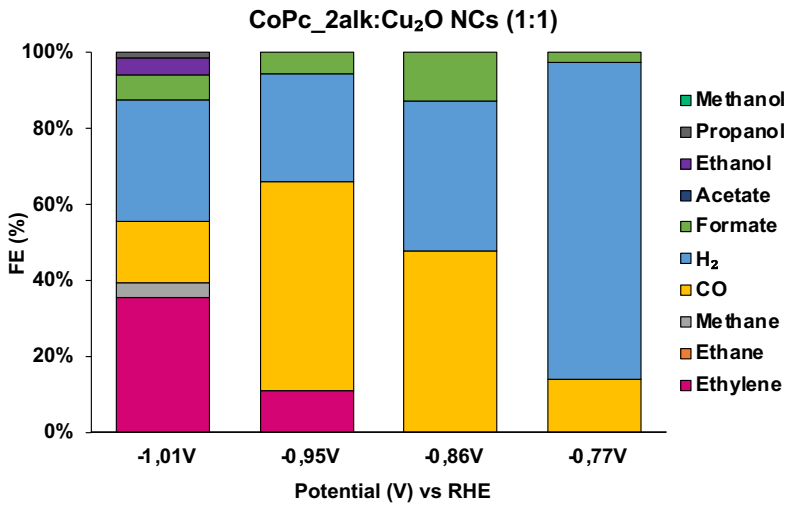

Figure 34. CoPc_2alk: Cu_2O (1:1) FE (%) at various applied potentials (V) vs RHE.

Figure 34 shows a product distribution similar to Cu_2O@CoPc_2Alk hybrid catalyst. However, ethylene production is noticeably higher, while CO formation is lower. Additionally, methanol is no longer detected, whereas ethanol and propanol are present. Overall, this system exhibits increased formation of C_{2+} products and a decrease in C_1 species. These results suggest that the absence of a core–shell structure does not promote strong cooperative behavior between the components, in this studied ratio. Otherwise, the higher ethylene production in the simple mixture indicates a greater C–C coupling, implying higher C_{2+} products formation.

A future work would focus on optimizing the polymer layer thickness in the hybrid systems and adjusting the composition ratio in the control experiments. It would also be valuable to test similar configurations using CNTs and the CoPc_3Alk polymer for further comparison.

6. CONCLUSIONS

In this study, an innovative strategy was developed to explore the tandem effect in CO_2RR by designing a core–shell hybrid system composed of Cu_2O NCs and a CoPc-based polymeric shell.

First, the Cu_2O NCs were synthesized and characterized by means of TEM, HRTEM-EDS, and XRD techniques, confirming their uniform cubic shape, size, and crystalline structure. These Cu_2O NCs were then electrochemically tested as a reference and starting point for this study, yielding a selectivity where H_2 and CO are predominant at low overpotentials, whereas the selectivity progressively shifts towards the formation of C_{2+} products upon increasing overpotentials.

Subsequently, two cobalt phthalocyanine-based polymers (CoPc_2alk and CoPc_3alk), were successfully synthesized via a "click" CuAAC polymerization reaction. On one hand, spectroscopic characterization (ATR-FTIR, UV-Vis, XPS) confirmed the formation of the polymeric matrix by revealing characteristic signals ascribable to the triazole moieties and CoPc. On the other hand, the electrochemical (CV, ECSA) characterizations indicated a higher intrinsic activity for CoPc_2Alk, suggesting a favorable polymeric architecture and spatial distribution arising from its di-substituted alkyne structure. Nevertheless, according to the electrochemical tests, both polymers demonstrated their potential as catalysts for the selective reduction of CO_2 to CO.

Moreover, both polymers were tested with CNTs to evaluate their performance within a higher-dispersed matrix. Notably, only the CoPc_2alk polymer exhibited enhanced catalytic activity, showing selective methanol production. This improvement highlights the impact of the polymerization process and its subsequent integration with CNTs, which together lead to enhanced dispersion and higher surface area.

Considering these results, the hybrid materials were synthesized by following the same strategy, employing Cu_2O NCs as templates and catalysts for in-situ core-shell formation. The characterization via TEM, HRTEM-EDS, ATR-FTIR, XRD, and XPS confirmed

successful core–shell formation while preserving the original structural features of the Cu_2O NCs. These hybrid catalysts were electrochemically tested under the same conditions, revealing a significant reduction in methane output, ethylene production exceeding 20%, and a shift in selectivity away from HER, which becomes less favorable at more negative potentials. In particular, Cu_2O@CoPc_2alk showed more pronounced suppression of hydrogen production than Cu_2O@CoPc_3alk, with higher CO production attributed to the higher electroactive surface area of the CoPc_2alk polymer. Although both hybrid systems suppress HER and promote CO generation, a substantial improvement in C–C coupling is not observed. This limitation may be due to the polymer layer's thickness, which likely hinders CO dimerization and allows intermediates to diffuse before the C-C coupling.

Further work should focus on a more in-depth study of the tandem effect between the polymers and Cu_2O NCs, particularly by reducing the thickness of the polymer shell to assess potential improvements in CO diffusion from the shell to the copper's surface. Additionally, this strategy opens up the route for alternative polymeric frameworks studies by tuning the monomeric species, which may enhance compatibility and catalytic properties, leading to more effective core–shell tandem systems.

7. AKNOWLEDGMENTS

Firstly, I sincerely thank ICIQ (Institute of Chemical Research of Catalonia) for allowing me to complete my master's thesis. This project wouldn't have been possible without their fellowship support, which enabled me to pursue the master's in Synthesis, Catalysis, and Molecular Design and conduct my research within the Palomares Group.

Secondly, I would like to thank my supervisor, Prof. Emilio Palomares, for his ongoing support, guidance, and encouragement throughout this journey. I would like to extend my acknowledgments to Joan Marc Bondia, PhD student, for his valuable assistance and mentorship throughout this work.

Thanks also go to Josep Manel Ricard, coordinator of the master's program, whose dedication made this program possible. I sincerely appreciate the support from the Scientific and Technical Resources Service (SRCiT) of the *Universitat Rovira i Virgili* (URV) for their technical assistance. Additionally, I want to thank project EQC2021-007785-P, funded by the Ministry of Science and Innovation and the European Union (NextGeneration), for the funding used to acquire the XPS system (ProvenX-NAP from SPECS) at the SRCiT of the URV.

Finally, I am grateful to all the members of the Palomares Group for their companionship and for creating an exceptional working environment. Thanks to my family and friends for their unwavering and unconditional support, which has been essential throughout my master's journey.

8. REFERENCES

(1) Nitopi, S.; Bertheussen, E.; Scott, S. B.; Liu, X.; Engstfeld, A. K.; Horch, S.; Seger, B.; Stephens, I. E. L.; Chan, K.; Hahn, C.; Nørskov, J. K.; Jaramillo, T. F.; Chorkendorff, I. Progress and Perspectives of Electrochemical CO_2 Reduction on Copper in Aqueous Electrolyte. *Chemical Reviews*. American Chemical Society June 26, **2019**, pp 7610–7672. https://doi.org/10.1021/acs.chemrev.8b00705.

(2) Lum, Y.; Yue, B.; Lobaccaro, P.; Bell, A. T.; Ager, J. W. Optimizing C-C Coupling on Oxide-Derived Copper Catalysts for Electrochemical CO_2 Reduction. *Journal of Physical Chemistry C* **2017**, *121* (26), 14191–14203. https://doi.org/10.1021/acs.jpcc.7b03673.

(3) Wang, Y.; Zhang, X.; Wei, Y.; Zhang, J. Boosting C_{2+} Selectivity in CO_2 Electroreduction on Cu Nanoparticles via Molecular Dispersion of Cobalt Phthalocyanine. *ChemCatChem* **2025**. https://doi.org/10.1002/cctc.202500056.

(4) Cheng, D.; Zhao, Z. J.; Zhang, G.; Yang, P.; Li, L.; Gao, H.; Liu, S.; Chang, X.; Chen, S.; Wang, T.; Ozin, G. A.; Liu, Z.; Gong, J. The Nature of Active Sites for Carbon Dioxide Electroreduction over Oxide-Derived Copper Catalysts. *Nat Commun* **2021**, *12* (1). https://doi.org/10.1038/s41467-020-20615-0.

(5) Zhang, B.; Wang, L.; Li, D.; Li, Z.; Bu, R.; Lu, Y. Tandem Strategy for Electrochemical CO_2 Reduction Reaction. *Chem Catalysis*. Cell Press December 15, **2022**, pp 3395–3429. https://doi.org/10.1016/j.checat.2022.10.017.

(6) Popović, S.; Smiljanić, M.; Jovanovič, P.; Vavra, J.; Buonsanti, R.; Hodnik, N. Stability and Degradation Mechanisms of Copper-Based Catalysts for Electrochemical CO_2 Reduction. *Angewandte Chemie - International Edition*. Wiley-VCH Verlag August 24, **2020**, pp 14736–14746. https://doi.org/10.1002/anie.202000617.

(7) Liu, T.; Sang, J.; Li, H.; Wei, P.; Zang, Y.; Wang, G. Towards Understanding of CO_2 Electroreduction to C_{2+} Products on Copper-Based Catalysts. *Battery Energy*. John Wiley and Sons Inc October 1, **2022**. https://doi.org/10.1002/bte2.20220012.

(8) Durand, W. J.; Peterson, A. A.; Studt, F.; Abild-Pedersen, F.; Norskov, J. K. Structure Effects on the Energetics of the Electrochemical Reduction of CO2 by Copper Surfaces. *Surf Sci* **2011**, *605*, 1354–1359.

(9) Han, N.; Wang, Y.; Ma, L.; Wen, J.; Li, J.; Zheng, H.; Nie, K.; Wang, X.; Zhao, F.; Li, Y.; Fan, J.; Zhong, J.; Wu, T.; Miller, D. J.; Lu, J.; Lee, S.-T.; Li, Y. Supported Cobalt Polyphthalocyanine for High-Performance Electrocatalytic CO_2 Reduction. *Chem* **2017**, *3*, 652–664.

(10) Feng, Q.; Sun, Y.; Gu, X.; Dong, Z. Advances of Cobalt Phthalocyanine in Electrocatalytic CO_2 Reduction to CO: A Mini Review. *Electrocatalysis*. Springer November 1, **2022**, pp 675–690. https://doi.org/10.1007/s12678-022-00766-y.

(11) Chen, T.; Li, M.; Liu, J. π-π Stacking Interaction: A Nondestructive and Facile Means in Material Engineering for Bioapplications. *Cryst Growth Des* **2018**, *18* (5), 2765–2783. https://doi.org/10.1021/acs.cgd.7b01503.

(12) Chen, X.; Wei, D.; Ahlquist, M. S. G. Aggregation and Significant Difference in Reactivity Therein: Blocking the CO_2-to-CH_3OH Reaction. *Organometallics* **2021**, *40* (17), 3087–3093. https://doi.org/10.1021/acs.organomet.1c00431.

(13) Garza, A. J.; Bell, A. T.; Head-Gordon, M. Mechanism of CO_2 Reduction at Copper Surfaces: Pathways to C_2 Products. *ACS Catal* **2018**, *8* (2), 1490–1499. https://doi.org/10.1021/acscatal.7b03477.

(14) Pandey, P.; Farha, O. K.; Spokoyny, A. M.; Mirkin, C. A.; Kanatzidis, M. G.; Hupp, J. T.; Nguyen, S. T. A "Click-Based" Porous Organic Polymer from Tetrahedral Building Blocks. *J Mater Chem* **2011**, *21* (6), 1700–1703. https://doi.org/10.1039/c0jm03483e.

(15) Kang, D.; Ko, J. H.; Choi, J.; Cho, K.; Lee, S. M.; Kim, H. J.; Ko, Y. J.; Park, K. H.; Son, S. U. Dual Role of Cu_2O Nanocubes as Templates and Networking Catalysts for Hollow and Microporous Fe-Porphyrin Networks. *Chemical Communications* **2017**, *53* (17), 2598–2601. https://doi.org/10.1039/c6cc10005h.

(16) Tang, C. Y.; Yang, Z. Transmission Electron Microscopy (TEM). In *Membrane Characterization*; Elsevier Inc., **2017**; pp 145–159. https://doi.org/10.1016/B978-0-444-63776-5.00008-5.

(17) Liu, G. L.; Kazarian, S. G. Recent Advances and Applications to Cultural Heritage Using ATR-FTIR Spectroscopy and ATR-FTIR Spectroscopic Imaging. *Analyst*. Royal Society of Chemistry March 30, **2022**, pp 1777–1797. https://doi.org/10.1039/d2an00005a.

(18) Kumar, P.; Joshi, C.; Srivastava, A. K.; Gupta, P.; Boukherroub, R.; Jain, S. L. Visible Light Assisted Photocatalytic [3 + 2] Azide-Alkyne “Click” Reaction for the Synthesis of 1,4-Substituted 1,2,3-Triazoles Using a Novel Bimetallic Ru-Mn Complex. *ACS Sustain Chem Eng* **2016**, *4* (1), 69–75. https://doi.org/10.1021/acssuschemeng.5b00653.

(19) Neti, V. S. P. K.; Wang, J.; Deng, S.; Echegoyen, L. High and Selective CO_2 Adsorption by a Phthalocyanine Nanoporous Polymer. *J Mater Chem A Mater* **2015**, *3* (19), 10284–10288. https://doi.org/10.1039/c5ta00587f.

(20) Guo, T.; Wang, X.; Ma, C.; Fu, Z.; Xing, X.; Bedane, A. H. Electrochemical CO_2 Reduction by Cobalt(II)2,9,16,23-Tetra(Amino)Phthalocyanine: Enhancement Effect of Active Sites toward Methanol Formation. *Energy and Fuels* **2024**, *38* (17), 16638–16656. https://doi.org/10.1021/acs.energyfuels.4c02354.

(21) Chauhan, A. Powder XRD Technique and Its Applications in Science and Technology. *J Anal Bioanal Tech* **2014**, *5* (6). https://doi.org/10.4172/2155-9872.1000212.

(22) Luo, H.; Li, B.; Ma, J. G.; Cheng, P. Surface Modification of Nano-Cu_2O for Controlling CO_2 Electrochemical Reduction to Ethylene and Syngas. *Angewandte Chemie - International Edition* **2022**, *61* (11). https://doi.org/10.1002/anie.202116736.

(23) Han, B.; Jin, Y.; Chen, B.; Zhou, W.; Yu, B.; Wei, C.; Wang, H.; Wang, K.; Chen, Y.; Chen, B.; Jiang, J. Maximizing Electroactive Sites in a Three-Dimensional Covalent Organic Framework for Significantly Improved Carbon Dioxide Reduction Electrocatalysis. *Angewandte Chemie - International Edition* **2022**, *61* (1). https://doi.org/10.1002/anie.202114244.

(24) Picollo, M.; Aceto, M.; Vitorino, T. UV-Vis Spectroscopy. *Physical Sciences Reviews* **2019**, *4* (4). https://doi.org/10.1515/psr-2018-0008.

(25) Ooyama, Y.; Yagi, S. *Progress in the Science of Functional Dyes*; Springer Singapore, **2021**. https://doi.org/10.1007/978-981-33-4392-4.

(26) Alessio, P.; De Oliveira, R. F.; Aoki, P. H. B.; Pereira, J. D. A. S.; Braunger, M. L.; Furini, L. N.; Vieira, M.; Teixeira, S. R.; Job, A. E.; Saenz, C. A. T.; Alves, N.; Olivati, C. A.; Constantino, C. J. L. Molecular Architecture and Electrical

Properties in Evaporated Films of Cobalt Phthalocyanine. *J Nanosci Nanotechnol* **2012**, *12* (9), 7010–7020. https://doi.org/10.1166/jnn.2012.6583.

(27) Greczynski, G.; Hultman, L. X-Ray Photoelectron Spectroscopy: Towards Reliable Binding Energy Referencing. *Progress in Materials Science*. Elsevier Ltd January 1, **202**0. https://doi.org/10.1016/j.pmatsci.2019.100591.

(28) Messias, I.; Winkler, M. E. G.; Costa, G. F.; Mariano, T.; Souza Junior, J. B.; Neckel, I. T.; Figueiredo, M. C.; Singh, N.; Nagao, R. Role of Structural and Compositional Changes of Cu_2O Nanocubes in Nitrate Electroreduction to Ammonia. *ACS Appl Energy Mater* **2024**. https://doi.org/10.1021/acsaem.4c02326.

(29) Fortgang, P.; Tite, T.; Barnier, V.; Zehani, N.; Maddi, C.; Lagarde, F.; Loir, A. S.; Jaffrezic-Renault, N.; Donnet, C.; Garrelie, F.; Chaix, C. Robust Electrografting on Self-Organized 3D Graphene Electrodes. *ACS Appl Mater Interfaces* **2016**, *8* (2), 1424–1433. https://doi.org/10.1021/acsami.5b10647.

(30) Glaser, T.; Peters, J. A.; Scharf, D.; Koert, U.; Dürr, M. Layer-by-Layer Deposition of Organic Molecules Controlled by Selective Click Reactions. *Chemistry of Materials* **2024**, *36* (1), 561–566. https://doi.org/10.1021/acs.chemmater.3c02707.

(31) De Riccardis, A.; Lee, M.; Kazantsev, R. V.; Garza, A. J.; Zeng, G.; Larson, D. M.; Clark, E. L.; Lobaccaro, P.; Burroughs, P. W. W.; Bloise, E.; Ager, J. W.; Bell, A. T.; Head-Gordon, M.; Mele, G.; Toma, F. M. Heterogenized Pyridine-Substituted Cobalt(II) Phthalocyanine Yields Reduction of CO_2 by Tuning the Electron Affinity of the Co Center. *ACS Applied Materials and Interfaces*. American Chemical Society February 5, **2020**, pp 5251–5258. https://doi.org/10.1021/acsami.9b18924.

(32) Chen, C.; Wang, M.; Zhang, Y.; Yang, X.; Zou, K.; Lin, W.; He, M.; Wu, H.; Han, B. Efficient CO_2 Electroreduction to N-Propanol on a Matching Cobalt Phthalocyanine/Copper Tandem Catalyst. *Green Chemistry* **2025**. https://doi.org/10.1039/d5gc00395d.

(33) Zhu, Q.; Rooney, C. L.; Shema, H.; Zeng, C.; Panetier, J. A.; Gross, E.; Wang, H.; Baker, L. R. The Solvation Environment of Molecularly Dispersed Cobalt Phthalocyanine Determines Methanol Selectivity during Electrocatalytic CO_2 Reduction. *Nat Catal* **2024**. https://doi.org/10.1038/s41929-024-01190-9.